

Estimation of NAPL-Water interfacial areas for unconsolidated porous media by kinetic interface sensitive (KIS) tracers

Alexandru Bogdan Tatomir¹, Huhao Gao², Christopher Pötzl², Nikolaos K. Karadimitriou³, Tobias Licha², Holger Class⁴, Rainer Herbert Helmig³, and Martin Sauter²

¹Uppsala University

²University of Göttingen

³University of Stuttgart

⁴Institut für Hydraulische Engineering

November 22, 2022

Abstract

Employing kinetic interface sensitive (KIS) tracers, we investigate three different types of glass-bead materials and two natural porous media systems to quantitatively characterize the influence of the porous-medium grain-, pore-size, and texture on the “mobile” interfacial area between an organic liquid and water. By interpreting the breakthrough curves (BTCs) of the reaction product of the KIS tracer hydrolysis we obtain a relationship for the specific interfacial area (IFA) and wetting saturation. The immiscible displacement process coupled with the reactive tracer transport across the fluid-fluid interface is simulated with a Darcy-scale numerical model. The results show that the current reactive transport model is not always capable to reproduce the breakthrough curves of tracer experiments and that a new theoretical framework is required.

Total solid surface area of the grains, i.e., grain surface roughness, is shown to have an important influence on the capillary-associated IFA by comparing results obtained from experiments with spherical glass beads having very small or even no surface roughness and those obtained from experiments with the natural sand. Furthermore, a linear relationship between the mobile capillary associated IFA and the inverse mean grain diameter can be established. The results are compared with the data collected from literature measured with high-resolution microtomography and partitioning tracer methods. The capillary associated IFA values are consistently smaller because KIS tracers measure the mobile part of the interface. Through this study, the applicability range of the KIS tracers is considerably expanded and the confidence in the robustness of the method is improved.

1 **Estimation of NAPL-Water interfacial areas for unconsolidated porous media by**
2 **kinetic interface sensitive (KIS) tracers**

3 **Alexandru Tatomir^{1,2}, Huhao Gao², Christopher Pötzl³, Nikolaos Karadimitriou⁴, Tobias**
4 **Licha⁵, Holger Class⁶, Rainer Helmig⁶, and Martin Sauter²**

5 ¹Department of Earth Sciences, Geocentrum, Uppsala University, Villavägen 16, 752 36 Uppsala,
6 Sweden.

7 ²Department of Applied Geology, Geoscience Centre of the University of Göttingen,
8 Goldschmidtstr. 3, 37077 Göttingen, Germany

9 ³Department of Structural Geology and Geodynamics, Geoscience Centre of the University of
10 Göttingen, Goldschmidtstr. 3, 37077 Göttingen, Germany

11 ⁴Department of Structural Engineering, University of Stuttgart, Pfaffenwaldring 7, 70569
12 Stuttgart, Germany

13 ⁵Department of Applied Geology, Institute of Geology, Mineralogy and Geophysics, Ruhr
14 University Bochum, Universitätsstr. 150, 44801 Bochum, Germany

15 ⁶Department of Hydromechanics and Modelling of Hydrosystems, University of Stuttgart,
16 Pfaffenwaldring 7, 70569 Stuttgart, Germany

17

18 Corresponding author: Alexandru Tatomir (alexandru.tatomir@geo.uu.se;
19 alexandru.tatomir@geo.uni-goettingen.de)

20

21 **Key Words:**

- 22 • Kinetic Interface Sensitive (KIS) tracers
23 • Fluid-fluid interfacial area
24 • Multiphase flow in porous media
25 • Reactive transport in porous media
26 • Immiscible displacement
27 • Column experiments
28 • Terminal menisci
29

30

31 Submitted to: *Water Resources Research*

32

33 **Abstract**

34 Employing kinetic interface sensitive (KIS) tracers, we investigate three different types of
35 glass-bead materials and two natural porous media systems to quantitatively characterize the
36 influence of the porous-medium grain-, pore-size and texture on the “mobile” interfacial area
37 between an organic liquid and water. By interpreting the breakthrough curves (BTCs) of the
38 reaction product of the KIS tracer hydrolysis we obtain a relationship for the specific interfacial
39 area (IFA) and wetting saturation. The immiscible displacement process coupled with the reactive
40 tracer transport across the fluid-fluid interface is simulated with a Darcy-scale numerical model.
41 The results show that the current reactive transport model is not always capable to reproduce the
42 breakthrough curves of tracer experiments and that a new theoretical framework is required.

43 Total solid surface area of the grains, i.e., grain surface roughness, is shown to have an
44 important influence on the capillary-associated IFA by comparing results obtained from
45 experiments with spherical glass beads having very small or even no surface roughness and those
46 obtained from experiments with the natural sand. Furthermore, a linear relationship between the
47 mobile capillary associated IFA and the inverse mean grain diameter can be established. The
48 results are compared with the data collected from literature measured with high resolution
49 microtomography and partitioning tracer methods. The capillary associated IFA values are
50 consistently smaller because KIS tracers measure the mobile part of the interface. Through this
51 study the applicability range of the KIS tracers is considerably expanded and the confidence in
52 the robustness of the method is improved.

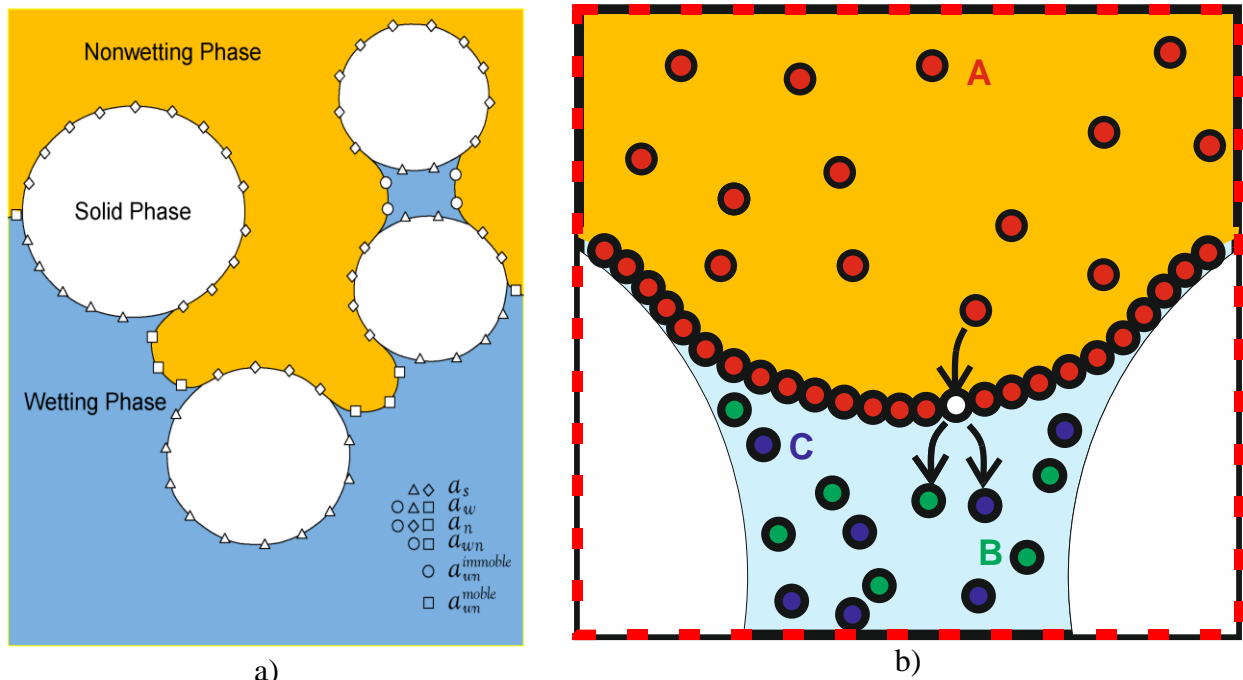
53

54 **1 Introduction**

55 The interfacial area between fluid-phases plays a critical role in the coupled multiphase
56 flow, solute transport and reaction processes in porous media (Miller et al. 1990; Hassanizadeh
57 and Gray 1990; Reeves and Celia 1996). Some applications, where the fluid-fluid interfacial area
58 (FIFA) plays a major role, are the geological storage of CO₂ (e.g., Niemi et al. 2016), oil and gas
59 recovery, the remediation of contaminated sites, such as per- and poly-fluoroalkyl substances
60 (PFAS) (e.g., Brusseau 2018; Brusseau 2019).

61 The fluid-fluid interfacial areas can be classified in capillary-associated interfacial areas
62 (IFAs) (e.g., menisci), and film-associated interfacial areas, or surface-adsorbed (Costanza-
63 Robinson and Brusseau 2002; Brusseau et al. 2006; Porter et al. 2010). The sum of the two
64 represents the total interfacial area. The capillary-associated IFA, a_{wn} , can be further subdivided
65 into immobile (or stagnant), $a_{wn}^{immobile}$, or mobile, a_{wn}^{mobile} (Figure 1) (Joekar-Niasar and
66 Hassanizadeh 2012a)

67



68 **Figure 1:** a) Illustration of the different types of interfacial areas b) KIS tracer (A) adsorption on
69 the fluid-fluid interface, followed by hydrolysis to form two by-products (B+C) dissolved
70 in water, an acid and alcohol.

71 **1.1 Models for calculating the FIFA**

72 Due to difficulties in directly measuring the FIFA, initial studies focused on developing
73 theoretical and modelling approaches employing normalized interfacial area per unit of
74 representative elementary volume (REV) (Leverett 1941; Gvirtsman and Roberts 1991;
75 Hassanizadeh and Gray 1993; Cary 1994; Reeves and Celia 1996; Bradford and Leij 1997; Held
76 and Celia 2001; Oostrom et al. 2001; Dalla et al. 2002; Dobson et al. 2006) The models can be
77 roughly classified into the following categories: pore-geometry models, where the porous media
78 is represented using an idealized spherical packing (e.g., Gvirtsman and Roberts 1991; Likos and
79 Jaafar 2013), or a bundle of capillary tubes (Cary 1994; Oostrom et al. 2001), and
80 thermodynamic-based models (Leverett 1941; Bradford and Leij 1997; Grant and Gerhard 2007)

81 measuring the net amount of reversible work. With the development of computational capabilities
82 other categories were added: pore-network models that use a simplified representation of the
83 porous media as a network of pore-bodies and pore-throats (Reeves and Celia 1996); pore-
84 morphology models (e.g., (Dalla et al. 2002); and direct pore-scale numerical simulations using
85 particle-based methods such as the Lattice Boltzmann (Porter et al. 2010), and smooth particle
86 hydrodynamics, and grid-based computational fluid dynamics methods such as the level-set-,
87 volume-of-fluid-, and phase field-methods (Gao et al. 2020). The pore-scale models calculate
88 explicitly the magnitude of FIFA and allow the calculation of upscaled per-volume normalized
89 quantities, i.e., capillary pressure, saturation and specific interfacial areas, required by the
90 continuum-based, Darcy-scale multiphase flow simulators. The expression of the FIFA as volume
91 averaged quantity allows its straightforward implementation into the Darcy-scale type flow
92 simulators since no additional parameters other than the initial ones are required.

93 **1.2 Measurement techniques for fluid-fluid interfacial area**

94 Several experimental methods were proposed to measure the fluid-fluid interfacial areas
95 (FIFAs): interface partitioning tracer test (IPTT), where the tracer is dissolved in aqueous (Kim et
96 al. 1997; Saripalli et al. 1997; Anwar et al. 2000; Brusseau et al. 2007) or in gaseous phase (Kim
97 et al. 1999; Costanza-Robinson and Brusseau 2002), high-resolution industrial X-ray
98 microtomography (XMT), and synchrotron XMT (Culligan et al. 2006; Brusseau et al. 2008;
99 Narter and Brusseau 2010; Porter et al. 2010; Peche et al. 2016; McDonald et al. 2016; Lyu Ying
100 et al. 2017; Patmonoaji et al. 2018; Araujo and Brusseau 2020), the gas adsorption chemical
101 reaction (GACR) (Lyu Ying et al. 2017), thin micro-models (Karadimitriou et al. 2016), and the
102 kinetic interface sensitive tracer method (Tatomir et al. 2018). The experimental methods for
103 measuring the FIFA are usually applied in controlled laboratory conditions, i.e. tracer methods,
104 XMT, micro models, (e.g., Dobson et al. 2006; Porter et al. 2010; Karadimitriou et al. 2016;
105 McDonald et al. 2016; Tatomir et al. 2018), but also in the field, i.e. tracer methods (Nelson and
106 Brusseau 1996; Annable et al. 1998; Simon and Brusseau 2007). Some methods are inherently
107 designed for laboratory conditions only, e.g. micro-models, and XMT.

108 Usually, standard tracer techniques measure the FIFA in steady state conditions, when a
109 residual saturation is formed. For instance, the gas-phase IPTT implies that a residual water
110 saturation is created in the column, while the gas phase together with two tracers, a conservative
111 and a reactive one, being circulated. The tracer partitioning on the fluid-fluid interface is
112 interpreted from breakthrough curves (BTCs) and the FIFA is calculated.

113 Most of the literature related to measurement of FIFA address to air-water fluid systems.
114 However, there is a consistent body of literatures which addresses to NAPL-water or organic
115 fluid-water fluid systems (Dobson et al. 2006; Schnaar and Brusseau 2006; Brusseau et al. 2008;
116 Brusseau et al. 2009; Narter and Brusseau 2010; Brusseau et al. 2010; Zhong et al. 2016; Tatomir
117 et al. 2018).

118 The kinetic interface sensitive (KIS) tracer method was proposed by Tatomir et al. (2018)
119 for quantifying the FIFA in a dynamic immiscible displacement process. A proof of concept was
120 provided using controlled column experiments with a well-characterized glass-bead porous
121 medium. The experimental results were interpreted by specifically developed numerical models
122 for multiphase flow coupled with reactive transport showing a general agreement of the FIFA
123 size with the theory. KIS tracers are first dissolved in the non-wetting phase and then injected.
124 When they come in contact with water, they hydrolyze to form two highly soluble components in
125 water, i.e., an acid and an alcohol. A KIS tracer stable component, with a zero-order reaction rate

126 was synthesized by Schaffer et al. (2013). The interpretation of the breakthrough curves of the
127 “byproduct acid” provides information about the size of the FIFA. Since the measurements are
128 performed for the tracer arriving at the outlet together with the mobilized water, KIS tracers are
129 considered to measure the mobile component of the capillary associated interface, a_{wn}^{mobile} .

130 **1.3 Studies comparing the experimental methods for FIFA measurement**

131 The magnitude of the FIFA reported in the literature depends on the measurement
132 technique employed. This is because it is not always clear which part of the FIFA a particular
133 technique measures, either the total interfacial area, the capillary-associated IFA, or some
134 combination of both the capillary-associated IFA and some part of the film associated area.

135 Thus, compared to aqueous-phase IPTT the gas-phase IPTT generally yields larger IFA
136 (Costanza-Robinson and Brusseau 2002). It is hypothesized that the gas-phase IPTT measures
137 both capillary and film-adsorbed FIFA while the aqueous-phase IPTT measure primarily FIFA
138 formed by water held by capillarity, e.g. pendular rings. At low water saturations the FIFA
139 measured with gas-phase IPTT showed exponential increase (Kim et al. 1999; Costanza-
140 Robinson and Brusseau 2002; Peng and Brusseau 2005). Similarly, using gas-phase IPTT, Peng
141 and Brusseau (2005) showed that at low water saturations, the maximum air-water IFA
142 approached those of the normalized solid surface areas, a_s . This indicates that indeed the gas
143 phase IPTT measure the total FIFA, as this was orders of magnitude larger than the calculated,
144 GSSA, but in good agreement with the SSSA measured with N₂/BET method.

145 Several studies reported that IPTT measured FIFAs were larger than those measured with
146 XMT, which can only scan with a certain resolution (Brusseau et al. 2006; Brusseau et al. 2007;
147 Brusseau et al. 2010; Brusseau et al. 2015; McDonald et al. 2016). Narter and Brusseau (2010)
148 compared the aqueous-phase IPTT with high-resolution micro-tomography for an organic liquid-
149 water -glass bead porous medium system, in an attempt to address the hypothesis that the surface
150 roughness has an influence on the FIFA. Their findings suggest that IPTT and micro-tomography
151 provide robust FIFA values that are comparable when the porous medium has no surface
152 roughness. In that sense, the maximum specific FIFA, was similar to the SSSA measured with
153 N₂/BET and using the smooth-sphere assumption. (Narter and Brusseau 2010; Zhong et al. 2016;
154 Lyu Ying et al. 2017). An explanation for this is that the computed micro-tomography measured
155 IFAs do not include areas associated with microscopic surface heterogeneities, i.e. roughness-
156 associated surface area (Brusseau et al. 2009; Brusseau et al. 2010). A review of the tracer-based
157 methods for measuring air-water IFAs is provided in (Costanza-Robinson and Brusseau 2002),
158 while the various sources of error of the IPTT are discussed in (Brusseau et al. 2008).

159 Note that relationships between the capillary associated IFA and the size of the total
160 interfacial area can be established. Grant and Gerhard (2007) used the previous pore-network
161 data of Dalla et al. (2002) to obtain the ratio of capillary-associated IFA to total IFA as a function
162 of the saturation. Thus, the total IFA obtained from their thermodynamic model is able to be
163 related to capillary-associated IFA for a given fluid saturation.

164 **1.4 Porous media characteristics influence on FIFA**

165 The size of FIFA is mediated by the pore-scale fluid configuration effects which are hard
166 to quantify. At the macro-scale, the FIFA is usually expressed as a function of fluid saturation.
167 Also, the capillary-associated IFA was observed to increase monotonically with increasing
168 capillary pressure and then to plateau at values that correspond to areas associated with residual
169 water saturation (Brusseau et al. 2006)

170 Literature studies have shown that porous medium texture influences the FIFAs, namely,
171 porous media with larger solid surface areas generate larger fluid-fluid interfacial areas. Several
172 studies demonstrate that fluid-fluid interfacial area is a function of soil properties such as **grain**
173 **size, grain size distribution, and surface roughness** (Cary 1994; Anwar et al. 2000; Peng and
174 Brusseau 2005; Cho and Annable 2005; Dobson et al. 2006; Brusseau et al. 2008; Brusseau et al.
175 2009; Brusseau et al. 2010; Jiang et al. 2020). In the following, the available studies of major
176 relevance on the influence of these parameters are described.
177

178 **1.4.1 Grain-size influence on fluid-fluid interfacial area**

179 Both the IFA models and experiments show that the maximum total specific FIFA is a
180 function of inverse median grain diameter (e.g., Anwar et al. 2000; Brusseau et al.
181 2009). Costanza and Brusseau (2000) used the theoretical model-based data reported by (Cary
182 1994) to evaluate the influence of porous-medium grain size on FIFA. One observation of these
183 studies was that porous media with smaller grain sizes have larger specific FIFAs. Using four
184 high purity sands (Dobson et al. 2006) conducted aqueous-phase interface-partitioning tracer tests
185 in NAPL-water fluid systems and compared the results with the theoretical models (Bradford and
186 Leij 1997; Oostrom et al. 2001) and a modified version of (Bradford and Leij 1997). Even though
187 the measured specific IFA were increasing with decreasing median grain diameter, not all the
188 reported experimental results (only three out of four) were following the theoretically expected
189 trend.

190 Brusseau et al. (2009) use ten porous media to study the influence of grain-size and
191 texture on FIFA. The results show that the specific FIFA and maximum specific FIFA correlate
192 very well with the inverse grain diameter. Also, the IFA correlates with SSSA and with the
193 inverse median grain diameter (IMGD). This, however, is obtained with tracer techniques which
194 are indirect measurement of IFA (Brusseau et al. 2009).

195 **1.4.2 Porous-medium-texture influence on the fluid-fluid interfacial area**

196 Besides the mean grain diameter, surface roughness is one of key parameters influencing
197 not only the fluid-fluid interface, but also the degree of wettability, the permeability of the
198 medium, or the capillary pressure- and relative permeability-saturation relationships.

199 Peng and Brusseau (2005) used the gas phase IPTT to measure the air-water FIFA for
200 eight soils and natural sands. The values were compared to the normalized surface areas of the
201 porous media. It was observed that FIFAs were generally larger for materials with larger SSSA
202 measured with N₂/BET method, incorporating the surface roughness.

203 Analyzing ten different types of porous media, comprising different grain-size
204 distributions and geochemical properties, Brusseau et al. (2009) report that grain-size
205 distributions have minimal impact on the FIFA. Brusseau et al. (2010) conducted aqueous phase
206 IPTT on two soils (Vinton and Eustis) and found that the maximum NAPL -water IFAs are much
207 larger than those obtained by geometric calculation with the smooth-sphere assumption (GSSA).
208 Their observations suggest that surface roughness has a significant impact on interfacial area and
209 that the glass beads' total specific IFA is similar to the SSSA predicted using the smooth-sphere
210 assumption. A linear relationship between the total solid area measured with N₂/BET and the
211 IPTT-measured IFA is established. However, this is based on a total of seven measurements, one
212 very large N₂/BET value being dominant. Because the film-associated areas are a significant
213 component of the FIFAs measured with IPTT, they conclude that the IPTT methods measure
214 some fraction of the interfacial area associated with surface roughness.

215 Zhong et al. (2016) used a modified version of aqueous-phase IPTT to measure FIFA for several
216 porous media made of glass beads, sand and Vinton soil during a series of drainage and

217 imbibition. The modified IPTT allows measuring the IFA at higher saturations than residual. The
218 maximum total FIFAs were compared to the SSSA measured with N₂/BET and to those estimated
219 based on GSSA.

220 Recently, Jiang et al. (2020) investigated the role of microscale surface roughness on the FIFA
221 assuming a triangular bundle-of-cylindrical capillaries, their model belonging to the pore-
222 geometry model category. The exponential increase of the total FIFA observed with the gas-
223 phase IPTT method when wetting saturation approaches zero can be explained by the impact of
224 surface roughness on the film-associated IFA.

225

226 **1.5 Objective**

227 To date, the KIS tracer method has been tested only for an ideal glass-bead well-sorted uniform
228 medium. An important step in the development of the KIS tracer method is the implementation of
229 the method for different soil types followed by the interpretation and comparison of the results.
230 Two categories of porous media are to be used, glass-beads and natural sands, having different
231 textures, grain- and pore-size distributions. By extending the applicability range of the KIS
232 tracers to several porous media, the generated set of tracer breakthrough curves is used,
233 subsequently, to verify the current modelling approaches.

234 For understanding the influence of **mean grain size, grain and pore-size distributions**, and
235 **surface roughness**, on the IFA, an extensive characterization of the glass beads and of the
236 natural sand is initially performed with digital image analysis and mercury intrusion porosimetry.
237 Our objective is to compare the IFA, obtained by KIS-tracer experiments in terms of the
238 maximum capillary associated specific interfacial area with published experimental data using
239 various measurement techniques and models.

240

241 **2 Materials and methods**

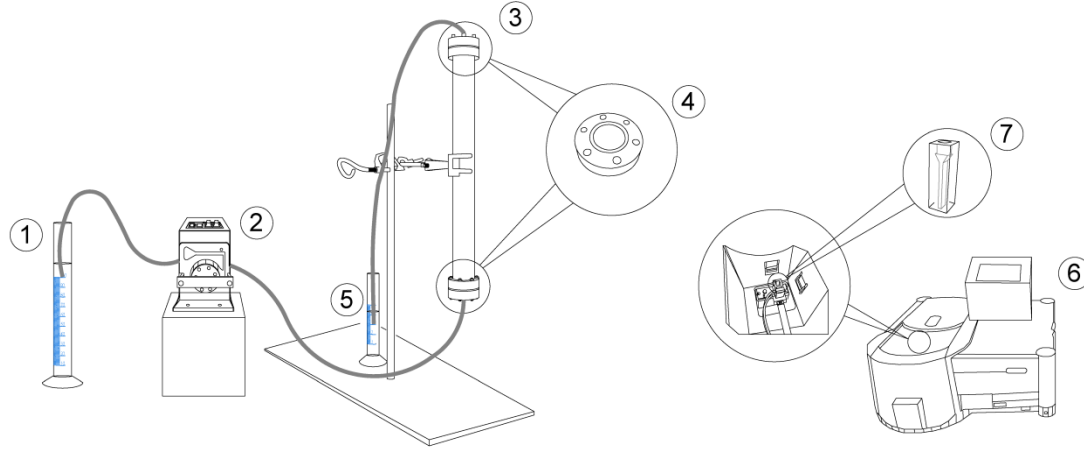
242 **2.1 Materials**

243 **2.1.1 Laboratory setup**

244 The testing procedure and experimental apparatus are those of our previous study (Tatomir et al.
245 2018). The experimental apparatus (Figure 2) consists of a stainless-steel column, 250 mm long
246 and 30 mm in diameter. Two metal frits with extremely fine meshes are placed either end of the
247 column holding the sand inside the column. A peristaltic pump with adjustable flow rate is first
248 used for saturating the column with water and later for providing a constant flow to the bottom of
249 the vertically oriented column of n-octane with dissolved KIS tracer. The peristaltic pump can set
250 the ratio of working power, but the actual flow rate depends on the permeability of the system.

251 The chemical stability of the materials (e.g., tubings, column) was tested in the presence of ultra-
252 pure water and n-octane. We observed that many carbon-based materials (i.e., tubings) interact
253 with the n-octane inducing either swelling or brittleness. Therefore, only materials which did not
254 react with n-octane were selected when constructing the experimental setup **Figure 2**.
255 Naphthalenesulfonates are highly fluorescent and can be detected at low concentration levels in
256 the range of µg/l using fluorescence spectrometry. The 2-NSA concentration in water was
257 measured using a Cary Eclipse fluorescence spectrophotometer from Varian Inc. The excitation
258 wavelength is 225 nm and the emission wavelength 338 nm.

259



260
 261 **Figure 2:** Experimental setup of two-phase flow system. 1) Reservoir of n-octane with KIS
 262 tracer. 2) Peristaltic pump. 3) Sand column. 4) Cap embedded with frit. 5) 5ml measuring
 263 cylinder. 6) Fluorescence spectrophotometer. 7) High precision fluorescence cuvette.

264
 265 **2.1.2 Porous media**

266 Five porous media – three glass-beads media and two natural sands - are used to investigate the
 267 influence of grain-size and texture on n-octane-water interfacial area. The relevant properties of
 268 the porous media are described in **Table 1**. Examples of microscopic images of the grains and the
 269 grain-size distributions obtained by digital image analysis performed on these images are shown
 270 in **Figure 3**. The images were processed using ImageJ software to determine the grain-diameters,
 271 roundness, Feret diameter, aspect ratio and circularity (Tatomir et al. 2016a). The three glass-
 272 bead porous media are a very fine sand (10-80 μm , $d_{50} = 55 \mu\text{m}$), a fine sand GB170 (120-230
 273 μm , $d_{50} = 170 \mu\text{m}$) and fine-to-medium sand GB240 (160-320 μm , $d_{50} = 240 \mu\text{m}$). GB240
 274 from GRACE (Glass beads 80/60 mesh) is very well sorted with the most uniformly distributed
 275 spectrum. The natural-sand porous media can be described as fine sand NS210, (120-320 μm ,
 276 $d_{50} = 210 \mu\text{m}$) and medium sand NS250 (180-380 μm , $d_{50} = 250 \mu\text{m}$).

277 The capillary pressure – saturation relationships were determined by mercury-intrusion
 278 porosimetry (MIP). To scale the relationships to the n-octane-water system, we used the contact
 279 angles, $\theta_{o,w}$, which were determined using digital image analysis (DIA) on microscopic images
 280 using the n-octane-water fluid system together with the grains of each porous media (**Table 1**).
 281 The conversion of an air-mercury system to an octane-water system is accomplished by
 282 rearranging Washburn relationship as given in eq. (1).

$$p_{c_{o,w}} = p_{c_{Hg,a}} \cdot \frac{\sigma_{o,w} \cdot \cos\theta_{o,w}}{\sigma_{Hg,a} \cdot \cos\theta_{Hg,a}} \quad (1)$$

283 where $p_{c_{w,o}}$, $p_{c_{Hg,a}}$, are the capillary pressure for the water-octane fluid system, mercury-air
 284 respectively. The mercury – air contact angle $\theta_{Hg,a}$ is 140° and $\sigma_{Hg,a}$ is $480 \text{ mN}\cdot\text{m}^{-1}$. $\sigma_{o,w}$, the
 285 interfacial tension of water-n-octane is $50.8 \text{ mN}\cdot\text{m}^{-1}$ at room temperature (Fukunishi et al. 1996).

286 The curves were fitted to those of the Brooks and Corey (1964) model by minimizing the root
 287 mean square error when determining the pore-size index λ , entry pressure p_e , and residual water
 288 saturation, S_{wr} in eq. (2):

$$p_c(S_w) = p_d \cdot \left(\frac{S_w - S_{wr}}{1 - S_{wr}} \right)^{-1/\lambda} \quad (2)$$

289 A high value of the pore index λ corresponds to a flat curve from the entry pressure, $S_w=1$, until
 290 reaching the residual saturation values, indicating the medium is well-sorted and implicitly the
 291 pore-throats are of similar size.

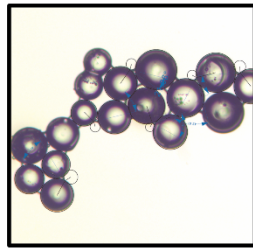
292 Analogously to the uniformity coefficient for grain size distributions, we propose a uniformity
 293 coefficient for the pores, defined as the ratio of $C_{pu} = p_{60}/p_{10}$, where p_{60} and p_{10} are the pore
 294 diameters corresponding to 60% and 10% finer on the cumulative pore-size distribution curve. A
 295 low C_{pu} signifies that the medium is composed of similar pore sizes, equivalent to being well-
 296 sorted. **Figure 4a** investigates the relationship between the mean pore diameter, p_{50} , the C_{pu} and
 297 the d_{50} . **Figure 4b** shows that the SSSA decreases almost linearly with the mean pore diameter.
 298 The distributions of the pores in each of the five materials are determined with mercury intrusion
 299 porosimetry, by applying the Washburn equation. The frequencies and cumulative distributions
 300 of the pore-size distributions are plotted in **Figure 5**. The glass beads are spherical and of
 301 uniform diameter and therefore, the theoretical specific solid surface area can be calculated using
 302 the smooth-sphere assumption expressed in (cm^{-1}) using eq. (3) or in (m^2/g), using eq. (4),
 303 (Costanza-Robinson and Brusseau 2002; Peng and Brusseau 2005):

$$GSSA(cm^{-1}) = \frac{6(1 - \phi)}{d_{50}} \quad (3)$$

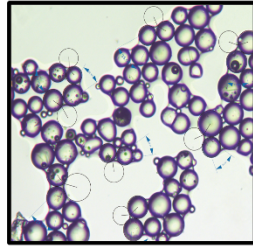
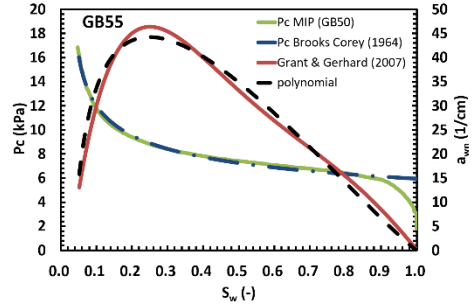
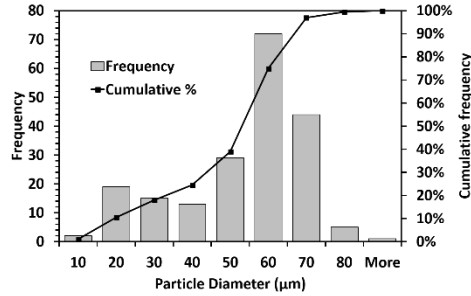
$$GSSA (m^2/g) = \frac{6}{d_{50} \cdot \rho_p} \quad (4)$$

304 where d_{50} , is the mean particle diameter (cm), ρ_p is the particle density which is 2.65 g cm^{-3} .

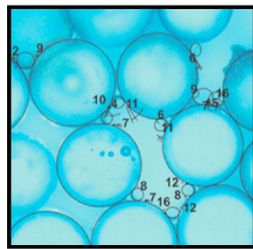
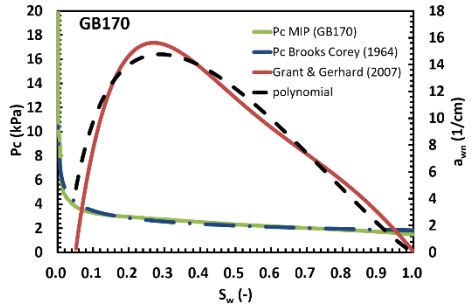
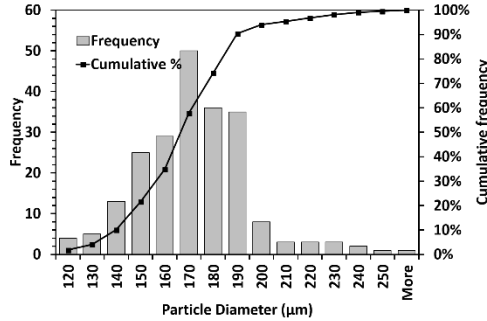
305 The theoretical total interfacial areas can be estimated based on geometrical calculations for
 306 smooth spheres and compared to the specific solid surface areas measured with the MIP method,
 307 SSSA-MIP.



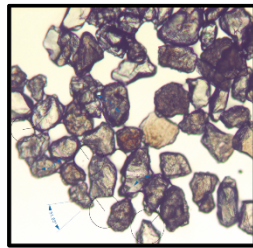
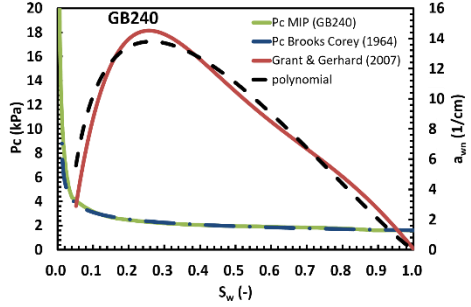
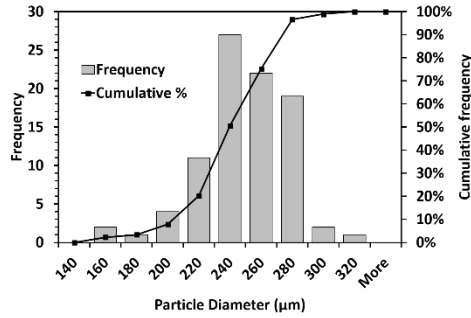
GB55



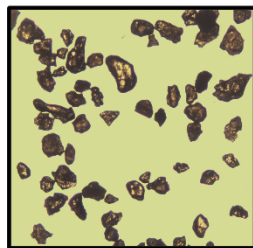
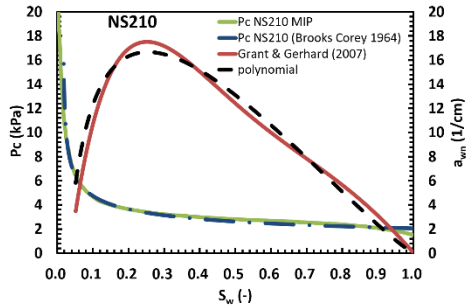
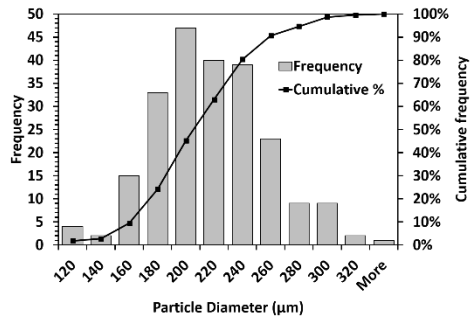
GB170



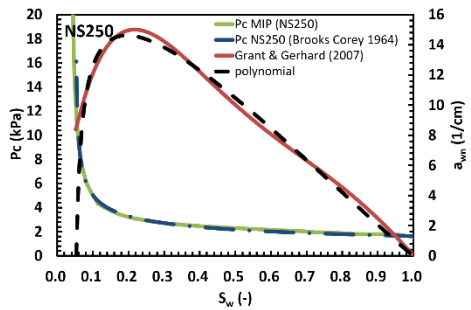
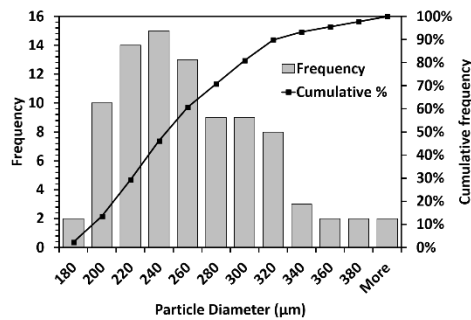
GB240



NS210



NS250



308

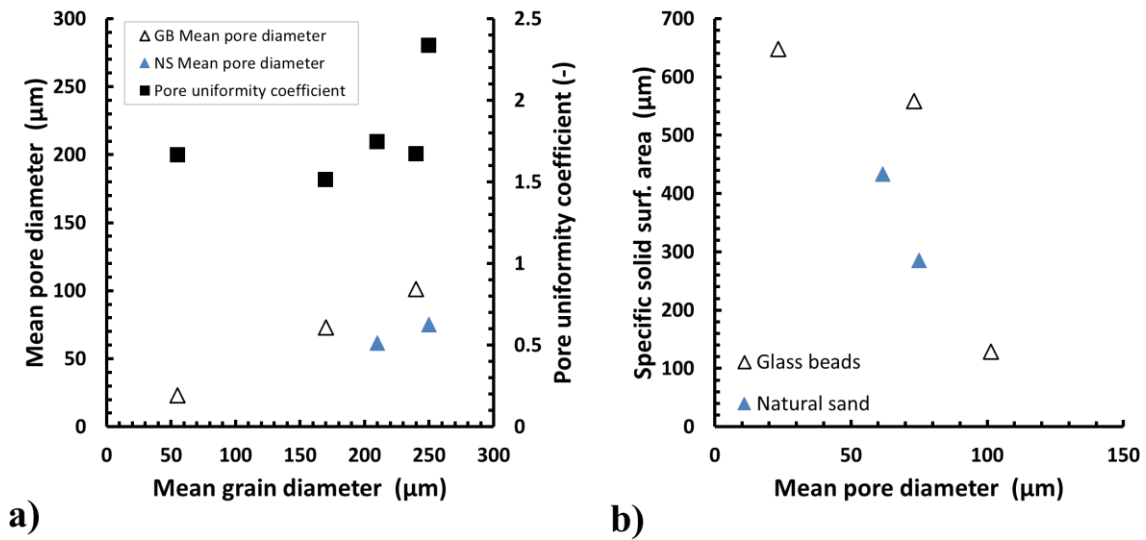
309

310

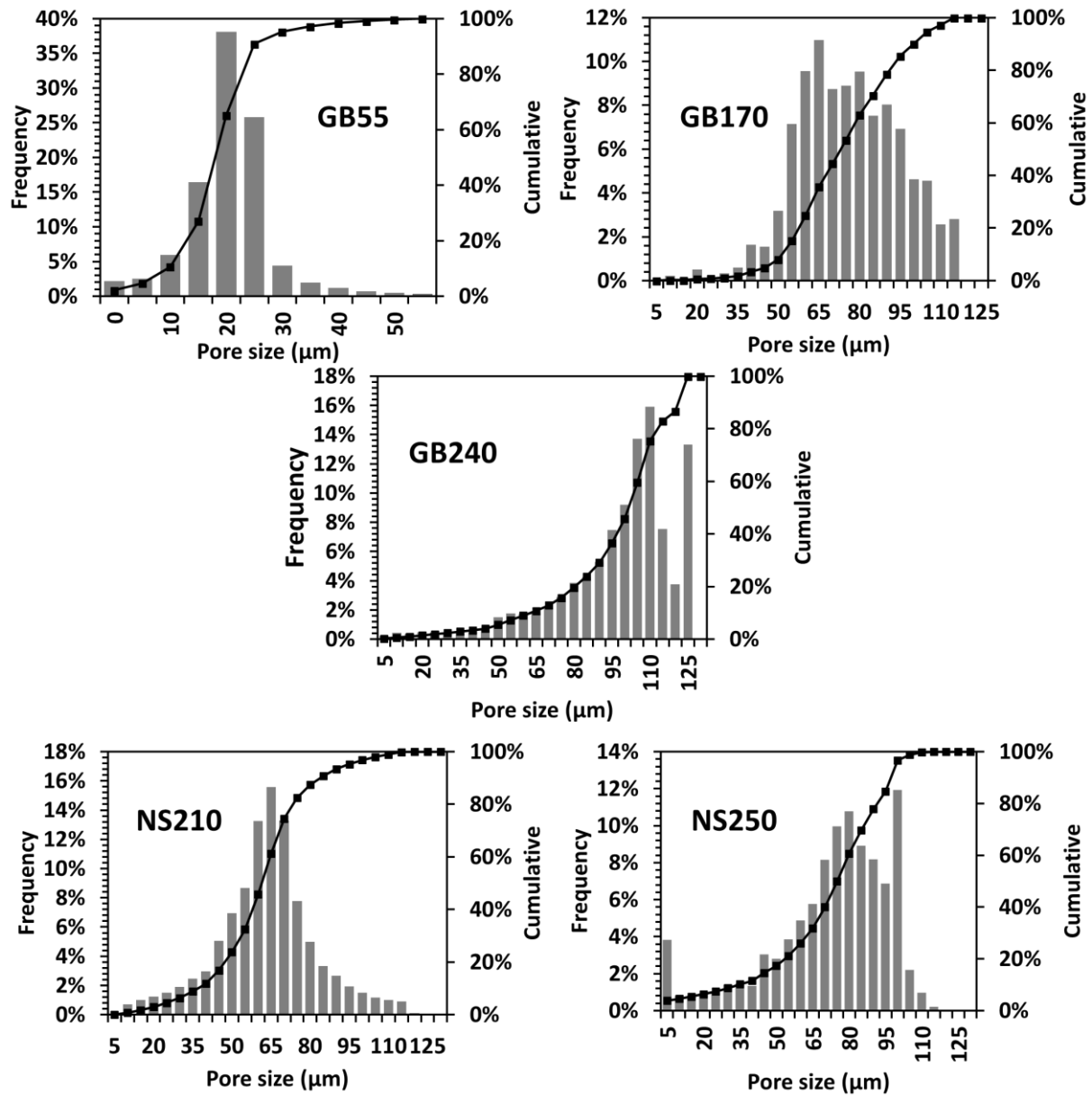
311

Figure 3: Characterization of the five porous media used in the KIS tracer experiments: three glass beads (GB55, GB170 and GB240) and two natural sands (NS210 and NS250). Digital illustration of the media (left column), grain-size (distribution) with the

312 cumulative frequency curve (middle), capillary pressure-saturation, $p_c - S_w$ relationship
 313 determined with MIP, and the calculated $a_{wn} - S_w$ relationship with the explicit
 314 interfacial area model of (Grant and Gerhard 2007)



315
 316 **Figure 4:** a) Relationship between mean pore-throat diameter (measured with MIP), p_{50} , pore
 317 pore uniformity coefficient ($C_{pu} = p_{60}/p_{10}$) and the mean grain diameter (measured with
 318 DIA), d_{50} ; b) The upper p_{50} values at GB55 and NS250 are corrected to remove the
 319 micro-porosity determined with MIP.



320
 321 **Figure 5:** Pore-diameter distribution determined with mercury-intrusion porosimetry, based on
 322 Washburn model (Washburn 1921)

323
 324 **Table 1.** Summary of relevant properties of the porous media used in the KIS tracer two-phase
 325 flow experiments

Parameter Name	Unit	Symbol	GB55	GB170	GB240	NS210	NS250
Porosity	(-)	ϕ	0.411	0.455	0.464	0.432	0.445
Intrinsic permeability	(m^2)	K	8e-13 – 2e-12	4e-12 – 1.1e-11	8e-12 – 1e-11	6e-13 – 8e-13	3e-12-9e- 12
d_{50} mean grain diameter	(μm)	d_{50}	55	167	240	206	248
d_{10}	(μm)	d_{10}	20	140	205	161	198

d_{60}	(μm)	d_{60}	57	172	244	214	258
Uniformity coefficient $C_u = d_{60} / d_{10}$	(-)	C_u	2.85	1.23	1.19	1.33	1.30
Mean pore diameter^a	(μm)	p_{50}	23.28	73.15	101.35	61.69	75.01
Pore uniformity coefficient^a $P_u = p_{60} / p_{10}$	(-)	P_u	1.67	1.51	1.67	1.75	2.34
SSSA- MIP (Rootare and Prenzlow 1967) $GSSA=6(1 - \phi)/d_{50}$	(cm^{-1})	a_s	615	558	128	419	274
Bulk density of the glass beads	(g/cm^3)	ρ_b	1.65	1.65	1.6	1.65	1.67
Lambda (Brooks-Corey)	(-)	λ	3.614	3.606	3.650	2.925	2.663
Contact angle n-octane - water	($^\circ$)	θ	32 \pm 6	34 \pm 9	10 \pm 3	32 \pm 10	32 \pm 10
Entry pressure	(Pa)	p_d	5937	1819	1606	2050	1642
Residual wetting phase saturation	(-)	S_{wr}	0.024	0.00	0.016	0.015	0.051
Longitudinal dispersivity	(m)	α_L	1e-3	1e-3	1e-3	1e-3	1e-3
Transversal dispersivity	(m)	α_T	1e-5	1e-5	1e-5	1e-5	1e-5
Feret diameter(mm)	(mm)		0.054	0.173	0.24	0.245	0.273
Circularity	(-)		0.857	0.855	0.898	0.676	0.593
Aspect ratio	(-)		1.062	1.065	1.018	1.457	1.59
Roundness	(-)		0.95	0.955	0.983	0.713	0.701

326 ^a Based on mercury intrusion porosimetry measurements

327 **Table 2:** Fluid and soil-fluid properties

Parameter Name	Unit	Symbol	Value/ Range
Diffusion coefficient	(m^2/s)	D_m	1e-9
Density water	(kg/m^3)	ρ_w	1000
Density n-octane	(kg/m^3)	ρ_n	703
Viscosity of water	($Pa \cdot s$)	μ_w	1.00e-03
Viscosity of n-octane	($Pa \cdot s$)	μ_n	5.42e-04
Surface tension n-octane - water^a	(N/m)	$\sigma_{o,w}$	0.0508
Longitudinal dispersivity^b	(m)	α_L	1e-3
Transversal dispersivity	(m)	α_T	1e-5

328 ^a Measurements of surface tension determined by capillary rise method showed no differences between pure n-octane and n-octane with 2g/l
329 dissolved KIS tracer

330 ^b Measured by single-phase tracer experiments in the column

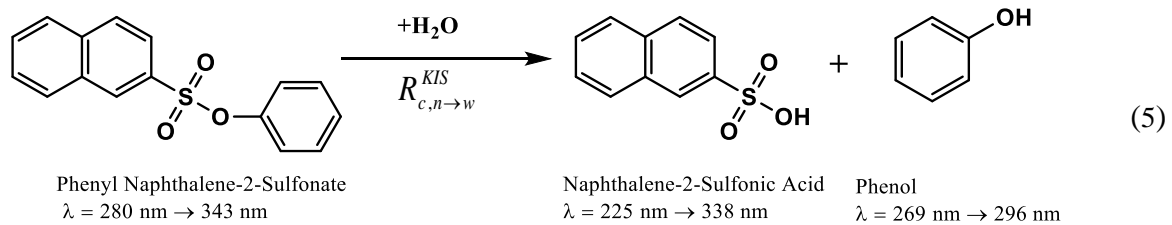
331

332 2.2 Methods

333 In this study the KIS tracer method is used to quantify the FIFA in several unconsolidated porous
334 materials. The KIS tracer experimental procedure was developed and described in Tatomir et al.
335 (2018). The technique consists of transient drainage experiments of an initially fully water
336 saturated porous media filled column. The drainage/invading fluid is n-octane with KIS tracer
337 dissolved in it. The laboratory experimental outcomes are volumetric outflow BTCs and KIS
338 tracer reaction product in water phase, i.e., 2-NSA concentration BTCs.

339 **2.2.1 KIS tracers**

340 KIS tracers, developed by Schaffer et al. (2013), are a category of non-polar, hydrolysable
341 phenolic esters. In contact with water they undergo an irreversible reaction at the fluid-fluid
342 interface to form two highly soluble products, i.e., an acid and an alcohol, Eq. (5). Their non-
343 polarity allows KIS tracers to be dissolved in non-polar liquids, e.g., n-octane. Due to the
344 pronounced fluorescent properties of their reaction products, the detection is performed by a
345 fluorescence spectrophotometer.



346 where $R_{c,n \rightarrow w}^{KIS}$, is the reaction rate constant, determined in static batch experiments.

347 The KIS tracer method was developed for tracking the FIFA in dynamic conditions (Tatomir et
348 al. 2018). Explicitly, the method is developed for the primary drainage process, i.e., non-wetting
349 phase displacing the wetting phase in a proof of concept study using well-characterized glass
350 beads in well-controlled laboratory conditions. By interpreting the volumetric ratios at outflow
351 and the reacted KIS tracer product acid breakthrough curves, we can derive the specific IFA
352 relationship of the fluid-fluid-porous media system.

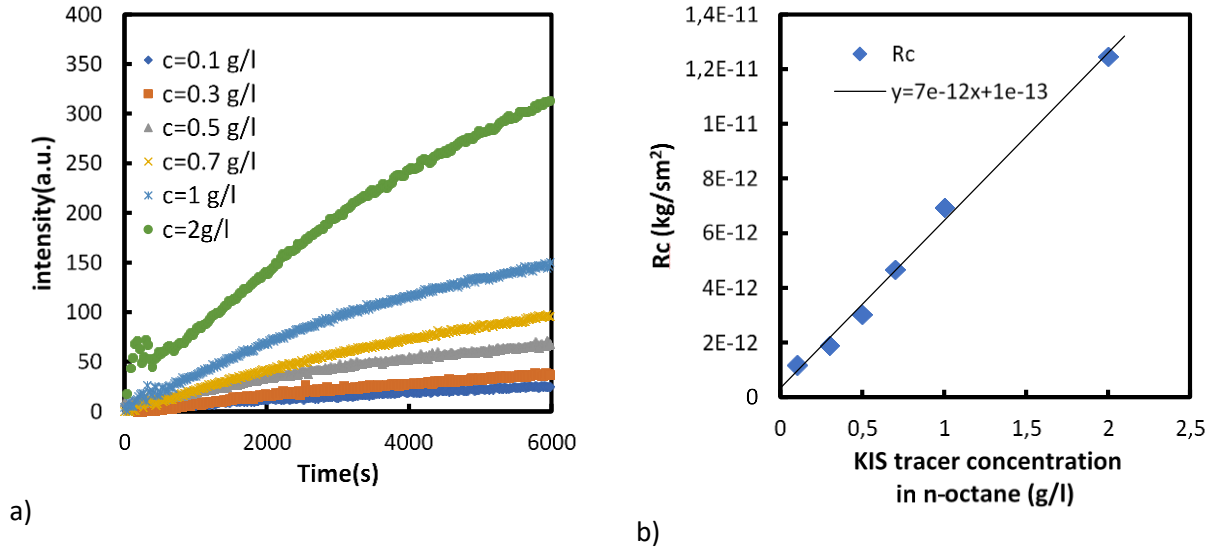
353 Note that the 2-NSA mass reacted in pendular rings of wetting fluid, around the contact points of
354 the porous media, cannot leave the column and is not being measured. Only the fraction of the
355 fluid-fluid interface belonging to the terminal menisci in contact with the continuous wetting
356 fluid body or mobile part is quantified by the KIS tracer technique.

357 **2.2.2 Kinetics of the tracer, new insights**

358 The KIS tracer hydrolysis reaction at the fluid-fluid interface was shown in static batch
359 experiments to lead to a linear increase of concentration after about 2000 – 3000 minutes
360 (Schaffer et al. 2013), independent on the initial KIS tracer concentration in the non-wetting
361 phase, i.e. n-octane. However, at the early stage (up to 100-200 minutes) was observed that the
362 reaction rate is increasing linearly depending on the initial concentration of the KIS tracer in the
363 non-wetting phase (**Figure 6**). With the pumping rates ranging between 0.3 and 1.5 ml/min one
364 column experiment usually takes around 6000 seconds. Therefore, the kinetic rates of the
365 experiment are the ones represented in **Figure 6b**). Generally, a higher reaction rate is preferable
366 to obtain higher 2NSA concentrations in water, because they can be better detected and measured
367 with the fluorescence spectrophotometer. Using an initial concentration of 2g/l KIS tracer, we
368 extend our previous range of testing which was 1g/l (Tatomir et al. 2018). It can be observed that
369 the resulting kinetic rate coefficient $R_{n \rightarrow w}^{2NSA} = 1.25 \cdot 10^{-11} \text{ kg} \cdot \text{m}^{-2} \cdot \text{s}$ follows very well the linear
370 behavior.

371 In this study, the experiments are conducted with an initial concentration of 0.5 g/l (all
372 experiments with GB55 and NS210, and two of the experiments with GB170) and 2g/l (all
373 experiments with GB240 and NS250 and one experiment with GB170) (**Figure 8**). Note that the

374 previous study (Tatomir et al. 2018) was conducted with the GB240 glass-bead medium with an
 375 initial KIS tracer concentration of 0.5g/l.



376
 377 **Figure 6:** Measured kinetic rates in static batch experiments. a) 2-NSA concentration reaction
 378 rates over time expressed in intensity units as a function of initial 2-NSA concentration
 379 in n-octane. b) calculated hydrolysis reaction rates as a function of initial 2-NSA
 380 concentration using the experiments in subfigure a). Here the unit of intensity $a.u. =$
 381 $86.293 \cdot c_{2NSA} + 62.6$

382 The hydrolysis reaction is expressed as:

$$-\frac{dc_{\alpha}^{\kappa}}{dt} = r_{n \rightarrow w}^{\kappa} = R_{c_{n \rightarrow w}^{\kappa}} \cdot a_{wn}, \quad (6)$$

383 where c_{α}^{κ} is the concentration of component κ in phase α , $R_{c_{n \rightarrow w}^{\kappa}}$ is the reaction rate constant.
 384 For component 2-NSA in water phase, $R_{c_{n \rightarrow w}^{2NSA}}$ was determined in static batch experiments
 385 (Figure 6). The a_{wn} is the capillary associated IFA. According to Joekar-Niasar and
 386 Hassanizadeh (2012) a_{wn} can be expressed using the polynomial expression in Eq. (7):

$$a_{wn}(S_w, p_c) = a_0(S_w)^{a_1}(1 - S_w)^{a_2}(p_c^{max} - p_c)^{a_3} \quad (7)$$

387 where a_{wn} is the capillary associated IFA, S_w is the wetting saturation, p_c is the capillary
 388 pressure, $a_0, a_1, a_2, a_3, p_c^{max}$ are empirically fitted parameters.

389 The transport of hydrolyzed KIS tracer in water, i.e. 2-NSA, is controlled by advection and
 390 diffusion processes.

391

392 2.2.3 NAPL-Water Experiments

393 The steel-column was packed with dry granular material (i.e. sand, or glass beads) using slight
 394 vibrations while packing to ensure uniform bulk properties. After packing the column is slowly
 395 filled with water from the bottom to avoid air entrapment. The columns are saturated for more

396 than 24 hours by pumping deaired ultra-pure deionized water. The porous medium properties are
397 reported in Table 1.

398 The 2-NSAPh (non-polar hydrolysable phenolic ester, phenyl naphthalene-2-sulphonate) in
399 concentrations of 0.5 g/l and 2g/l in the n-octane, is used as the KIS tracer. Approximately 30 ml
400 of the solution is then injected into the column at a rate between 0.4 and 0.8 ml/min. At the outlet
401 the two-phase flow breakthrough curve (BTC) was captured by collecting the fluid volumes in 5
402 ml graded measuring cylinder. Using a glass syringe, the water containing reacted KIS tracer is
403 taken and placed in a 500 μ l cuvette to be analyzed in the spectrophotometer. A predefined
404 calibration curve allows the conversion of intensity readings into 2-NSA concentration (**Figure**
405 **6**). After the analysis, the water is collected in 5-ml vials. Initially, at the outlet, only water is
406 being drained from the system. Just before the arrival of the first n-octane at the outlet, the
407 sampling intervals are taken more often for a higher temporal resolution of the BTC. The
408 sampling frequency is dictated by the minimum volume of water required to fill the cuvette that
409 is placed in the spectrophotometer.

410 After every experiment the glass beads and the natural sands are washed and dried for more than
411 48 h. The porous steel frits of the columns are washed and dried before each experiment and the
412 packing process repeated. However, each packing will lead to a different grain geometric
413 configuration, which may lead to differences in petrophysical parameters, i.e. permeability,
414 tortuosity with little influence on porosity.

415 **2.2.4 Data analysis: Mathematical modelling and interpretation of the results**

416 The interpretation of the experimental results is done using numerical modeling. The
417 mathematical and numerical model to handle the column-scale, i.e. Darcy (REV) scale, is an
418 immiscible two-phase flow model with reactive transport and it accounts for the specific IFA
419 (Tatomir et al. 2018). The mathematical model is implemented in COMSOL Multiphysics v5.5.
420 Several models capable of addressing the KIS tracers in multiphase flow in porous-media
421 systems were developed in the past (Tatomir et al. 2013; Tatomir et al. 2015; Tatomir et al.
422 2016b; Tatomir et al. 2018). Besides the immiscible two-phase flow models, a compositional
423 model investigating the KIS tracer application in supercritical CO₂ – brine fluid systems was
424 developed in the DuMu^X simulator (Flemisch et al. 2011; Tatomir et al. 2015). Comparing the
425 two models applied with experimental data, Tatomir et al. (2018) showed only minor differences.
426 In this study, the results were interpreted with the COMSOL implemented model only.

427 A two-step approach is employed to interpret the results. The first step is the calibration of the
428 two-phase flow model to the experiment by performing a sensitivity analysis with respect to flow
429 rate, Q , and intrinsic permeability, K . It is estimated that both have the highest measurement
430 uncertainty, due to the expected small oscillations in the pumping rate (± 0.05 ml/min) and the
431 unknown influence of repacking the columns, and of the column frits. The peristaltic pump is set
432 to operate at a fixed number of rotations per minute. As pressure in the column and the n-octane
433 reservoir at the inlet changes during the experiment, flow rate fluctuations can be expected. The
434 permeabilities of the sand are determined by falling head permeameter, which may provide a
435 wide range of permeability values. Adding to the uncertainty of the permeability measurement is
436 the effect of the porous frits and of repacking before each experiment.

437 Once the outflow volume ratio curves are matched, we proceed with the calibration of the
438 concentration breakthrough curves of the KIS tracer reaction product, i.e. 2-NSA. In this sense, a
439 sensitivity analysis using the specific interfacial-area relationship, $a_{wn} - S_w$, as the unknown
440 parameter is conducted. The reaction rate expressed in Eq. (6) depends on the reaction rate
441 coefficient, known from experiments and on a_{wn} . Initially, the Grant and Gerhard (2007)
442 thermodynamically derived model is used to approximate the specific IFA a_{wn} curves from the
443 MIP measured $p_c - S_w$ relationships. Afterwards, the polynomial expression in Eq. (7) is used to
444 fit the modelled a_{wn} , by finding best fitting parameters, a_0, a_1, a_2, p_c^{max} . This provides the
445 theoretical $a_{wn} - S_w$ of the fluid-fluid porous medium system.

446 The second step comprises the calibration of the KIS reaction product breakthrough curves. This
447 is performed running a parameter sweep on parameter a_0 in Eq. (7). This parameter controls the
448 maximum specific IFA, a_{wn}^{max} while maintaining the general shape of the $S_w - a_{wn}$ curve.

449 The solute dispersivities were determined using fluorescent tracer experiments to be 10^{-3} m
450 (Tatomir et al. 2018). Note that dispersivities measured in single-phase flow conditions is not
451 necessarily valid when another fluid-phase is present (Karadimitriou et al. 2016). Applying the
452 root mean square error (RMSE) as a criterion the best fitting curves were found.

453 In order to compare with the experimental and modelling BTC curves, the modelling results are
454 post-processed. The volumetric ratios of the non-wetting phase to total fluid measured at the
455 outlet are integrated over the sampling intervals, to obtain the values at the times when the
456 samples were taken. For further details of the mathematical models, see Tatomir et al. (2018)
457 proof of concept study.

458 **3 Results**

459 The experimental and modelling results for the three sets of tests performed on each of the five
460 porous media, three glass beads, GB55, GB170, GB240, and two natural sands, NS210, NS250,
461 are presented in section 3 and discussed in section 4.

462

463 **3.1 Two-phase flow calibration**

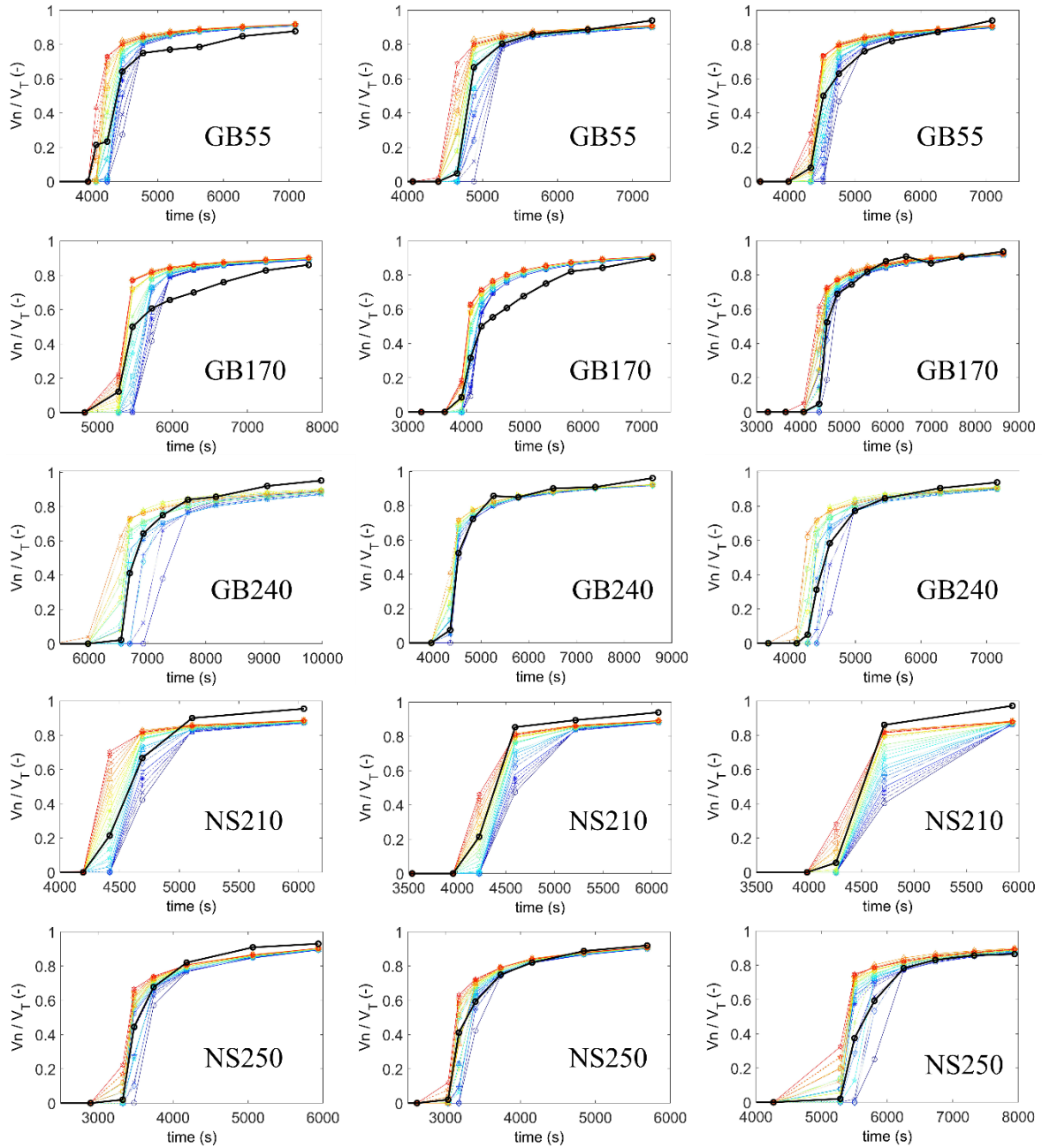
464 All fifteen experimental breakthrough curves (BTCs) of the volume fraction of the non-wetting
465 phase to total fluid volume together with the model calibration BTCs are illustrated in **Figure 7**.
466 The modelling parameters determined from the petrophysical characterization of the natural
467 sands and glass beads samples are reported in Table 1 and of the fluid system in Table 2.

468 First, we calibrate the immiscible two-phase flow model by performing the parameter sweep with
469 a combination of flow rates and permeabilities. The fitting of the modelling results to the
470 experimental data is shown in **Figure 7**. It can be observed that the two-phase flow model can
471 well match the experimental breakthrough curve, with the root mean square errors ranging up to
472 0.057 for the best fitting model curves, as showed in **Table SI 1**. Deviations are found mainly in
473 two experiments performed with GB170, where the change in the non-wetting to total volumetric
474 ratio at breakthrough is gentler in the experimental data compared to that of the modelled

475 breakthrough. In contrast, for NS210, the non-wetting phase breakthrough is fast and only little
476 water volume is being displaced out of the column, leading to a smaller number of data points.
477 This becomes apparent in the increase of non-wetting to total volume ratio at breakthrough
478 occurring more rapidly in the experimental BTC than the modelled ones.

479 Even though the frits are washed and dried before each experiment and the packing processing
480 follows the exact same procedure (vibrating and adding small increments) for each experiment,
481 differences are hard to avoid. The reproducibility of the experiments is mainly affected by
482 repacking and by the frits condition, which are reflected by the overall permeability of the
483 system. Therefore, the calculated flow rates and permeabilities in **Table SI 1** for the three
484 experiments belonging to each sand category are slightly different.

485



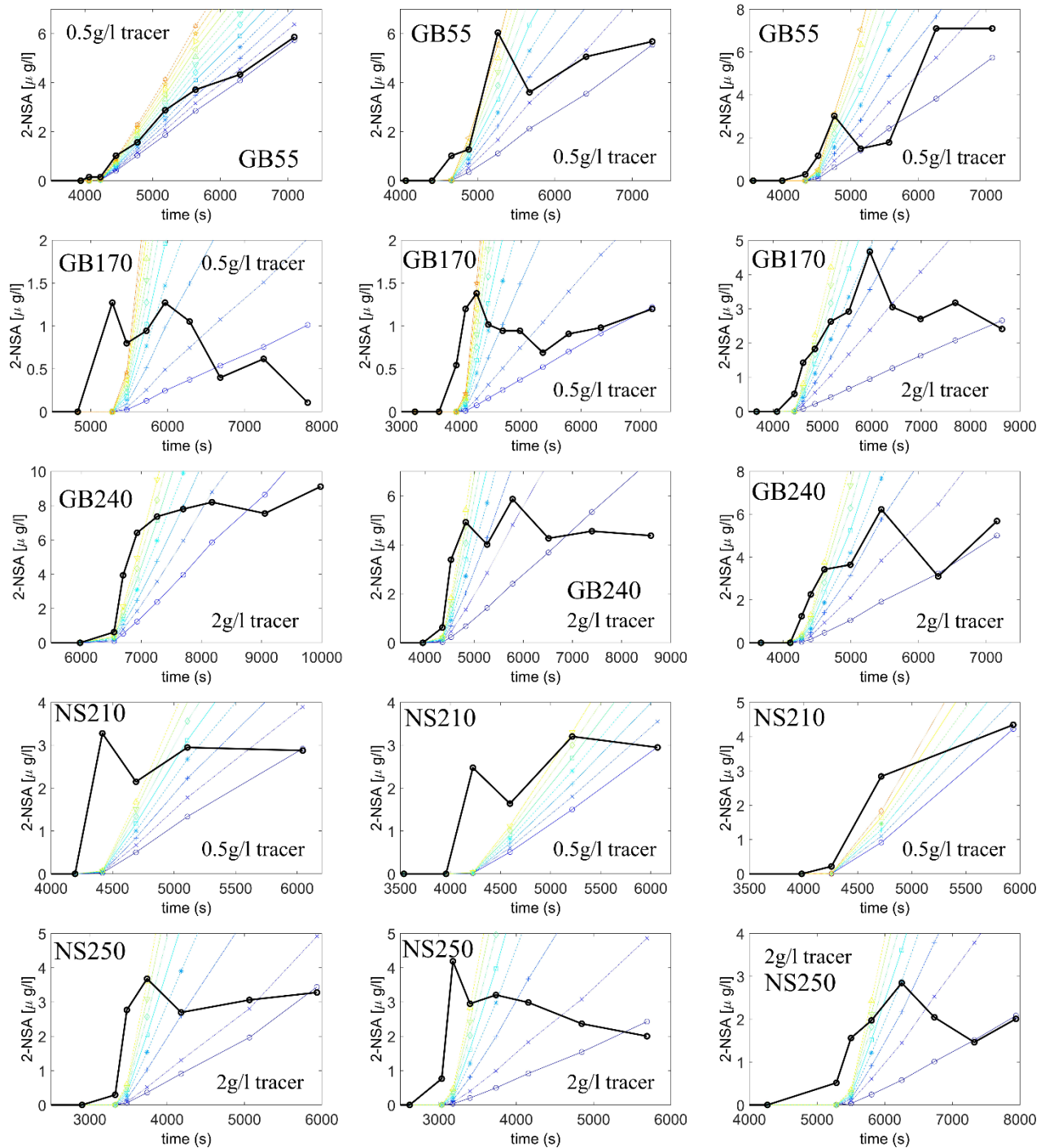
486

487 **Figure 7:** Breakthrough of the volumetric fraction of non-wetting phase to total fluid volume at
 488 the column outlet, experimental data (black) and simulated breakthrough curves with
 489 sensitivity analysis (color). The variation ranges are provided in **Table SI 1**

490

491

492 **3.2 Interpretation of the hydrolyzed KIS tracer reaction product breakthrough**
 493 **curves**



494
 495 **Figure 8:** Breakthrough curve of 2-NSA concentration (hydrolyzed KIS tracer) at column outlet.
 496 The black curve shows the experimental-data, while the colored plots correspond to a
 497 range of fitting coefficient a_0 , varied between $a_{0,min}$ and $a_{0,max}$ (yellow) given in **Table**
 498 **3**. The initial KIS tracer concentration in n-octane is specified in each subfigure

500 **Table 3:** Parameters ranges, $a_{0,min}$ to $a_{0,max}$ used to identify the best fitting for the capillary-
501 associated IFA, a_{wn} in Eq. (7). Here $a_{0,GG}$ and $a_{0,BF}$ are the a_0 parameter best fit to the Grant
502 and Gerhard (2007) model, and to the experimental data

Soil category	$a_{0,min}$	$a_{0,max}$	$a_{0,GG}$	$a_{0,BF}$	a_1	a_2	a_3	p_c^{max} (Pa)
GB55	9.67×10^{-6}	4×10^{-5}	5.22×10^{-5}	1.33×10^{-5}	0	1.11	1.94	23287
GB170	4×10^{-6}	7.33×10^{-5}	5.23×10^{-5}	6.67×10^{-6}	0	1.21	2.18	5749
GB240	1×10^{-5}	8×10^{-5}	5.31×10^{-5}	1.33×10^{-5}	0	1.15	2.14	5804
NS210	3.5×10^{-6}	8.5×10^{-5}	5.95×10^{-5}	4.33×10^{-5}	0	1.15	2	9466
NS250	5.33×10^{-6}	6×10^{-5}	6.06×10^{-5}	6.33×10^{-6}	0	1.05	1.83	15491

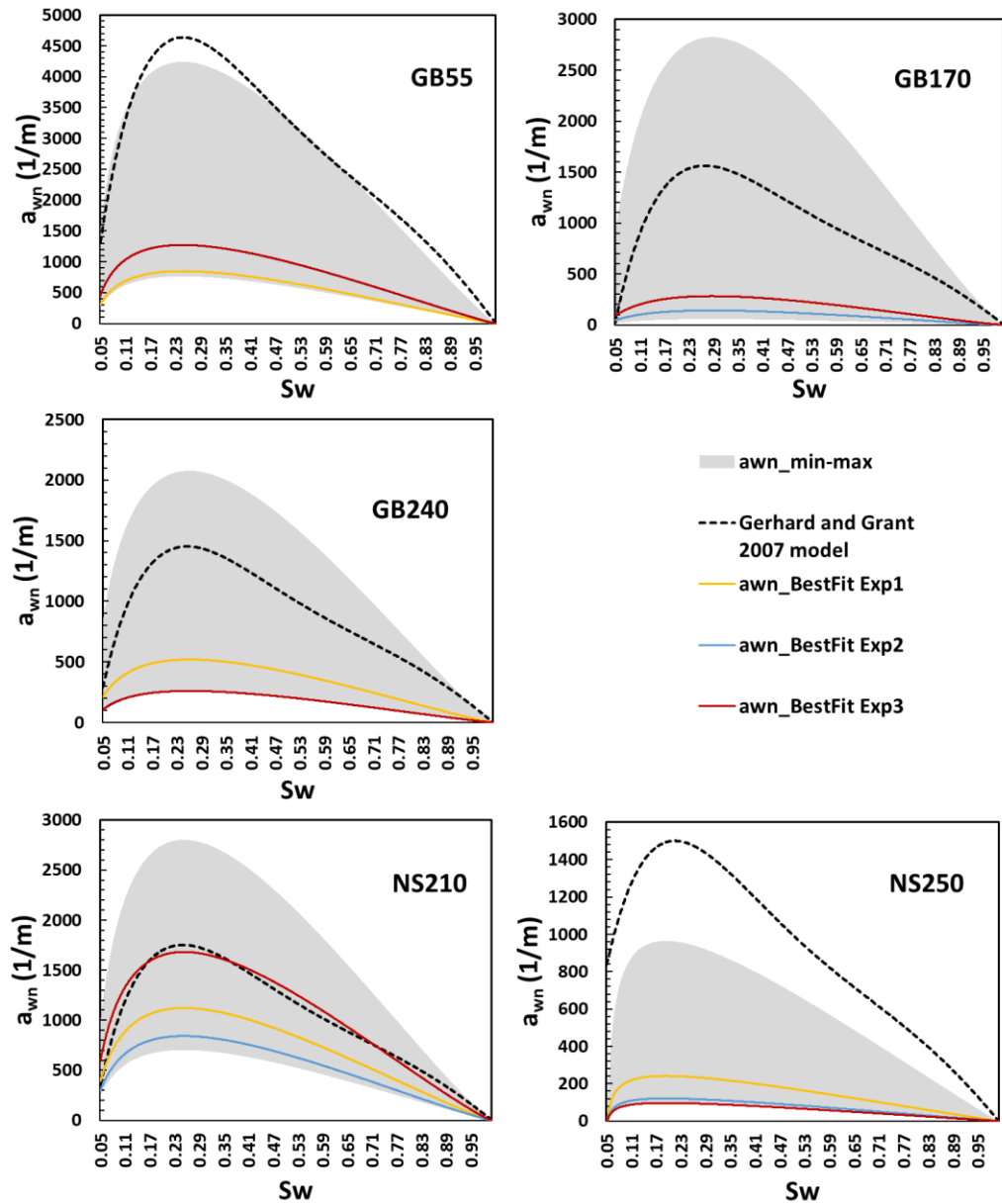
503
504 The breakthrough curves of the reacted 2-NSA concentration are plotted in Figure 8. Measured 2-
505 NSA concentrations in water range between 0 and 8 $\mu\text{g/l}$. With a constant kinetic rate dependent
506 on the initial tracer concentration in n-octane (Figure 1), the mass transfer across the fluid-fluid
507 interface is a function of only fluid-fluid interfacial area. In order to obtain the range of the
508 specific interfacial area when fitting to the experimental data, the parameter a_0 in the polynomial
509 equation (7) is swapped to change the magnitude of the $a_{wn} - S_w$ curve while maintaining the
510 shape of the curve (Tatomir et al. 2018). The calculated root mean square error ranges between
511 0.3 and 2.3 for the best fitting parameter a_0 , as shown in **Table SI 1**. Compared to the non-
512 wetting phase fluid to total volume ratio BTCs calibration, the modelled 2-NSA BTCs have a
513 larger deviation from the experimental data. Generally, the trend of the BTCs is ascending.
514 However, a clear linearly increasing trend, as it is predicted by the numerical models, is not
515 always seen in the experimental data. This indicates that either we deal with a systematic
516 experimental error, or the theoretical framework underlying the current coupled two-phase flow
517 and reactive-transport model needs to be reconsidered. This is further addressed in the discussion.

518 3.3 Capillary-associated specific interfacial area calculation

519 The range of the $a_{wn} - S_w$ curves and the best fitting curves found for the five porous materials
520 are illustrated in Figure 9 with gray shading. The gray shading corresponds to the range of a_0
521 values (Table 3) that scale the $a_{wn} - S_w$ curves so that all experimental data points of the 2-NSA
522 BTCs in Figure 8 are captured. The maximum $a_{0,max}$ values correspond to the peak matching the
523 first points on the BTC, the curve with steepest slope, while the minimum, $a_{0,min}$, corresponds to
524 the curves matching the points on the tailing of the BTC. Once a_0 is determined, the a_{wn}^{max} value
525 can be obtained from the $a_{wn}(S_w)$ curve, which usually exists at water saturation ranging
526 between 0.2 and 0.35. The best fitting a_0 values, $a_{0,BF}$, obtained on grounds of RMSE are given
527 in **Table SI 1** together with the a_{wn}^{max} and the RMSE values and are plotted in Figure 10.

528 The a_{wn} predicted by the explicit IFA model of Grant and Gerhard (2007), using the MIP
529 $p_c - S_w$ curves is within the areas resulting from the interpretation of the 2-NSA tracer
530 breakthrough curves, for all grains, except for the natural sand NS250. In this case, the Grant and
531 Gerhard (GG) model overestimates the a_{wn} . Generally, the GG model provides larger FFA than

532 those providing the best fit resulting from the tracer interpretation. For NS210 the best fit of the
 533 third experiment matches almost exactly the GG model. On average the GG model predicts
 534 a_{wn} values that can be even five times larger than those obtained for the model best fits.



535
 536 **Figure 9:** Ranges for the specific capillary associated IFA, $a_{wn} - S_w$ relationships, for the five
 537 porous media. The best fitting curves in each experiment (Exp.1 - yellow, Exp.2 - blue,
 538 Exp.3 - red), and the Gerhard and Grant model applied to MIP derived $p_c - S_w$ curves

539 4 Discussion

540 Assuming two fluid phases inside the porous medium as being stagnant. Since there is no force
 541 applied, the IFA between the fluids remains constant and the KIS tracer hydrolysis over the fluid-
 542 fluid interface produces a steady increase of the 2-NSA concentration in water. As time passes,

543 the 2-NSA concentration diffuses away from the fluid-fluid interface with the only driving force
544 of the process being the concentration gradient, i.e., molecular Brownian motion. When the non-
545 wetting phase starts to displace the wetting phase, a transition zone is formed, where saturation
546 changes with time. During this process, only the tracer concentration in water in direct proximity
547 to the outflow is measured. In other words, only the interfaces belonging to the front can
548 contribute to the measured concentration at the outlet. The longer the two fluids remain in contact
549 the higher the outlet concentration should be. In reality, the pore distribution inside the column
550 forms complex geometrical patterns. The macro-scale displacement front is in fact formed of
551 fingers following various tortuous pathways.

552 Therefore, an early arrival of the concentration peak corresponds to a larger number of fingers
553 arriving at the outlet, which are followed by other fingers that are halted due to the presence of a
554 confinement in the pore space, and the competitive domination of fingers occupying smaller
555 pores than the first ones that, combined, result in a lower outlet concentration. Some of the
556 fingers may also mobilize water in the capillaries which may eventually be pushed to regions that
557 are stagnant. In these regions the advective transport flux is almost zero. The water in these
558 regions never reaches the outlet and, implicitly, the corresponding concentration is never
559 measured. Visualization of the mobile and immobile zones can be done for instance in thin
560 transparent (quasi-) two-dimensional micromodels (Karadimitriou et al. 2016). In a few words,
561 the effects taking place on the pore scale can and will affect the corresponding outflow
562 concentration and, given the experimental setup, it is physically impossible to identify the pore-
563 scale filling sequence mechanism.

564 The immiscible displacement can be studied as a function of the capillary number, $Ca = v\mu_i/\sigma$
565 and the viscosity ratio $M = \mu_i/\mu_d$ (Lenormand et al. 1988), where v is the velocity of the
566 invading fluid, μ_i and μ_d are the dynamic viscosities of the invading and displaced fluids, and σ
567 is the interfacial tension between the two fluids. A stable front means that the transition zone
568 (width) is constant in time. If the displacing or the invading fluid is less viscous than the
569 displaced fluid the front tends to become unstable. In our case $M = 0.5$ and the Ca of the fifteen
570 experiments is between 0.4 and 3.5 (Appendix SI Table 1). When M gets smaller, preferential
571 flow starts to occur, increasing the lengths and widths of the transition zone (e.g., Heiß et al.
572 2011). For the KIS tracer experiments, a stable front having a narrow transition zone will lead to
573 fewer measurement points than compared to those induced by an unstable flow with a large
574 transition zone. The NS210 experiments have the highest Ca numbers, 2.58, 2.7 and 3.6 while the
575 NS250 the lowest, i.e., 0.34, 0.59 and 0.62 (Table SI 2). For NS210 the BTCs have maximum 4
576 measurements, while in for NS250 the minimum number of points is 6.

577 **4.1 Hydrolyzed KIS tracer breakthrough curves**

578 Examining the 2-NSA breakthrough curves in **Figure 8**, the two main differences between
579 modelled and experimental results are: First, after phase breakthrough for most of experiments
580 (11 out of 15), the BTCs exhibit an early concentration peak immediately after the first arrival,

581 usually within the first three sampling times. The second difference is the deviation of the
582 experimental BTC from a straight line. They have a non-linear behavior characterized by a
583 slower increase in concentration, or even by a decrease at late times (i.e., first experiment GB170,
584 second experiment NS250). The concentration peak and the concentration decrease are not
585 present in the BTC predicted by the models but the breakthrough curves appear as straight lines.
586 In fact, such effects cannot be reproduced by our current model. Closest to the predicted linear
587 trend of the reactive transport model are the BTCs for the GB55. The curves consist of more than
588 6 measurement points.

589 With the lowest grain-uniformity coefficient, C_u , value of 1.19, GB240 is the most uniform
590 medium, closest to an ideal mono-size medium. RMSE values for of the GB240 obtained when
591 matching the volumetric ratios BTCs during the two-phase flow model calibration are the lowest
592 of the five materials. The three GB240 experiments are conducted with an initial KIS tracer
593 concentration of 2g/l. The same glass beads were used in our previous study (Tatomir et al.
594 2018), where we ran four experiments with an initial KIS tracer concentration of 0.5 g/l. In
595 comparison to our previous study where the BTCs had maximum four measurement points, the
596 BTCs have now eight measurement points. Two of the four results in (Tatomir et al. 2018)
597 provided a narrow a_{wn}^{max} range, i.e., 4.1 -5.4 cm^{-1} , 5.0 -7.5 cm^{-1} , and the other two large a_{wn}^{max}
598 ranges, i.e. 3.0-15 and 4.6 – 11.5 cm^{-1} . The best fitted results in **Table SI 1** give a_{wn}^{max} ranges
599 between 2.6 – 5.19 cm^{-1} which can be considered in good agreement with our previous set of
600 experiments.

601 Generally speaking, the confidence in measurements increases when a larger number of
602 measurement points is available. Even though the first GB170 experiment has eight measurement
603 points the BTC presents a clear descending trend, while the other two experiments tend to flatten
604 out.

605 From Figure 9 the largest a_{wn}^{max} error range, i.e. $a_{wn}^{max}(a_{0,max}) - a_{wn}^{max}(a_{0,min})$ is encountered for
606 the GB55, 8.2 - 42.4 cm^{-1} . Excluding the GB55, the natural sands with a larger surface roughness
607 do not have a larger range of a_{wn}^{max} than the glass beads. The calculated IFAs range for natural
608 sands is 13.99 cm^{-1} for NS210, 13.19 cm^{-1} for NS250 is smaller than that of the glass beads, 34.2
609 cm^{-1} for GB55, 19.55 cm^{-1} for GB170 and 18.2 cm^{-1} for GB240.

610 **4.2 Potential explanations of discrepancies in tracer BTC**

611 The discrepancies between the modelled and experimental results are believed to highlight the
612 complexity of the coupled multiphase flow and reactive transport processes. The shape of 2-NSA
613 concentration BTCs highly depend on the front behavior when it reaches the outlet. Once being at
614 the outlet the non-wetting phase is continuous, while in the domain entrapped regions of wetting
615 fluid were formed. Let us consider the porous medium being as a bundle of capillaries. Those
616 with the largest apertures/radii are the capillaries first invaded by the non-wetting phase in the
617 displacement process. Should these capillaries represent the largest part, it becomes clear why a
618 concentration peak arrives at the beginning of BTC, just ahead of the fluid-fluid interface

619 reaching the outlet. For a continuum-scale model, assuming the medium as homogeneous, such
620 type of preferential flow will be averaged.

621 An early breakthrough peak and other discrepancies could also be explained by artefacts resulting
622 from injection and sampling procedures. Concentration ranges are small, below 10 $\mu\text{g/l}$, i.e.,
623 experimental errors could also be expected. Care was taken when conducting the experiments and
624 several procedures were tried and repeated, and therefore, we do not consider experimental errors
625 and artefacts as a likely reason for the discrepancies.

626 The parametric study on a_0 values used to scale the $a_{wn} - S_w$ curves covers all experimental
627 data points of the 2-NSA BTCs in Figure 9. Therefore, it is reasonable to assume that one of the
628 $a_{wn} - S_w$ represents the “true” solution. One can see that the theoretical model of Grant and
629 Gerhard (2007) is in four cases within the parameter range, even providing an exact match for the
630 third experiment with NS210. This indicates the specific IFAs measured with KIS tracer method
631 are within a reasonable range.

632 **4.3 Grain-diameter-size influence on IFA**

633 Previous literature studies, reviewed in the introduction, revealed that the total specific IFA, a_n ,
634 and its related, a_{wn} , are inversely proportional to the mean grain size (Brusseau et al. 2009;
635 Brusseau et al. 2010). They observe very strong correlation between total specific interfacial area
636 and IMGD. Furthermore, a_n , was observed to have a linear dependency on water saturation. It
637 decreases linearly with S_w , $a_n = a_n^{max}(1 - S_w)$, where the a_n^{max} is the maximum total specific
638 interfacial area. The a_n^{max} was shown to be approximately equal with the solid surface area (a_s)
639 (Porter et al. 2010; Brusseau et al. 2010). The value of a_n is shown to be smaller for smooth glass
640 beads and larger for natural sands, or soils, (e.g., Brusseau et al. 2009). The curve is reported to
641 have virtually no hysteresis, somewhat unexpected as since the $a_{nw} - S_w$ curves present
642 hysteresis.

643 We found that GB55 has a much larger specific interfacial area compared to GB170 and GB240.
644 The largest specific IFA is recorded for NS210. This implies that materials with smaller grain
645 diameters will have larger specific interfacial area.

646 **4.3.1 Determination of maximum specific capillary-associated interfacial area with the** 647 **KIS tracer method**

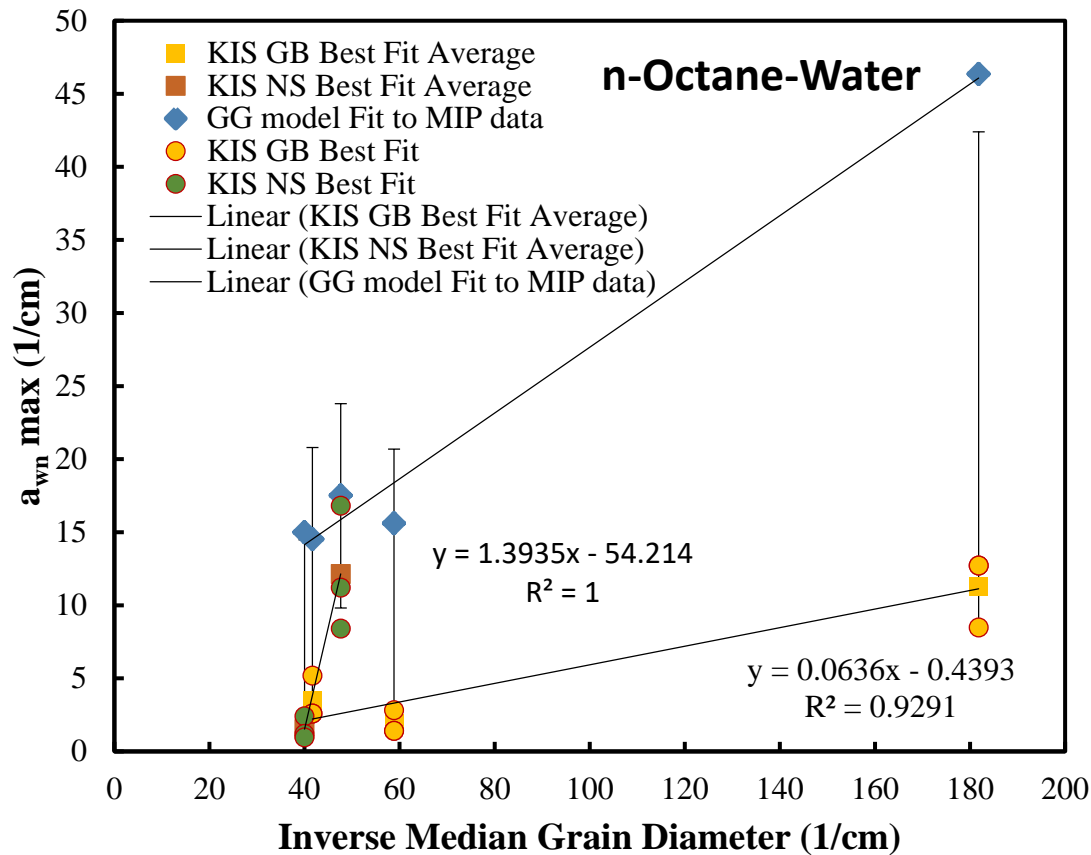
648 In Figure 10 the maximum values for specific capillary associated IFA, a_{nw}^{max} , obtained with KIS
649 tracer method are plotted. We plot the three sets of a_{nw}^{max} obtained for each soil category, the
650 average value and the error range corresponding to the minimum and maximum a_0 values.
651 Implementing a linear regression line over the $a_{nw}^{max} - IMGD$ data we obtain the following
652 relation for the glass-beads material:

$$a_{wn}^{max} = 0.0636/d_{50} - 0.4393 \quad (8)$$

653 Similar to values reported in the literature for total maximum total FFA, a_n^{max} , the a_{wn}^{max} follows
654 a linearly increasing trend with an increase in IMGD. There is a clear distinction between the

655 slopes of the linear regression lines of natural sand materials and glass beads. Having a larger
 656 surface roughness than the glass beads, the natural sand a_{wn}^{max} has a much larger increase in slope
 657 with IMGD.

658 The capillary-associated IFAs of the five materials determined with the thermodynamically based
 659 explicit IFA model (Grant and Gerhard 2007), follow a linear relationship $a_{wn}^{max, GG}$ when plotted
 660 against the IMGD. In this case no discrepancy between the natural sands and glass beads is
 661 observed.



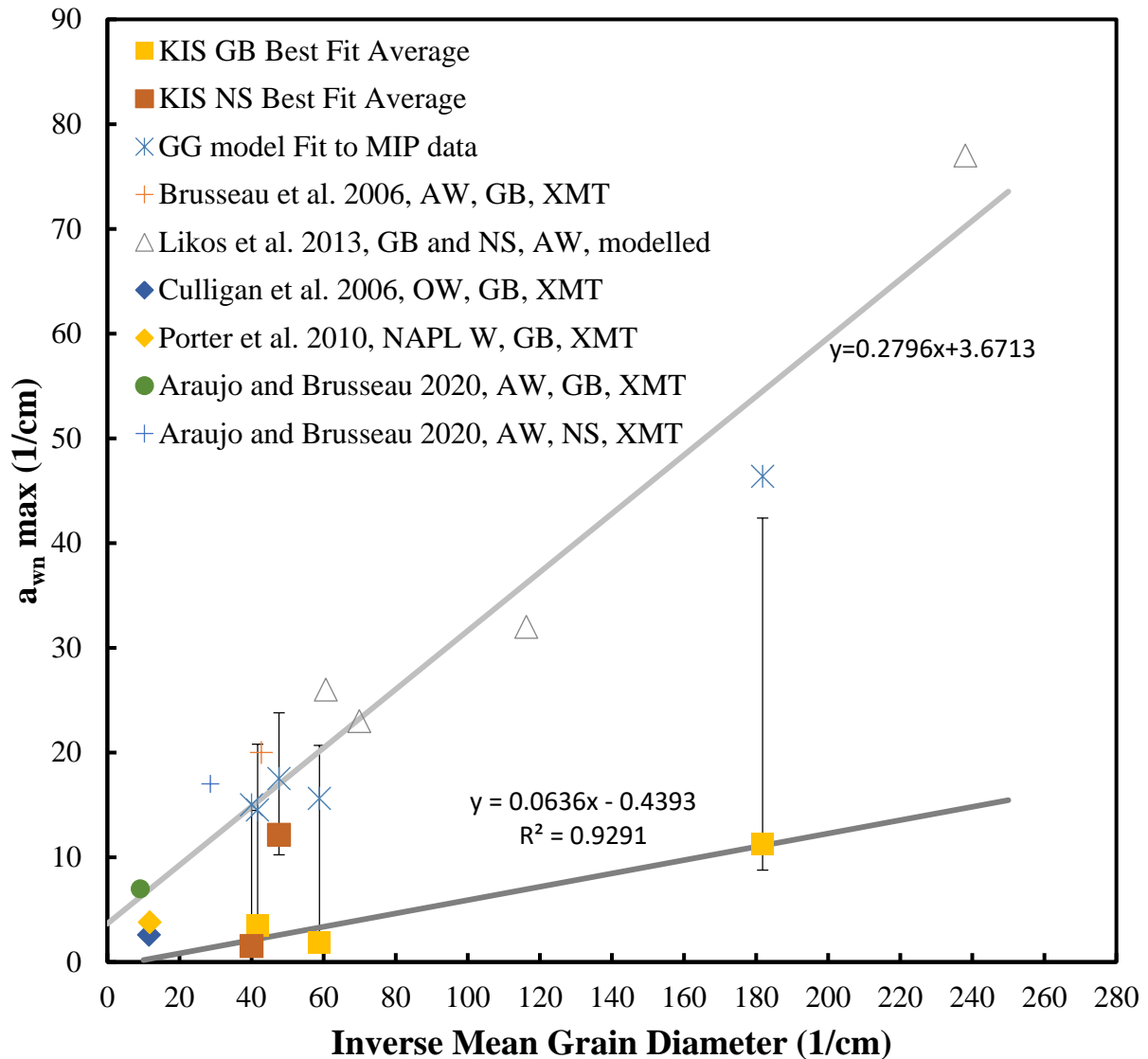
662
 663 **Figure 10:** Relationship between n-octane/water maximum specific capillary associated
 664 interfacial area, a_{wn}^{max} and inverse median grain diameter. Values determined using the
 665 KIS tracers on the five porous media, GB55, GB170, GB240, NS210, NS250. The values
 666 for a_{nw}^{max} are reported in **Table SI 1**.

667 **4.3.2 Comparison of maximum capillary associated-specific interfacial area with**
 668 **literature**

669 The comparison of FIFA with the literature data needs to account first for the type of IFA being
 670 compared, i.e. total or capillary associated IFA, and for the different porous media-fluid system
 671 types. Most commonly, the fluid-systems used in the reported experiments are air-water and, less
 672 often, NAPL-water. To the authors' knowledge there are only four studies that report the
 673 measured specific capillary associated IFA (Culligan et al. 2006; Brusseau et al. 2006; Porter et
 674 al. 2010; Araujo and Brusseau 2020). XMT was used in each of these studies.

675 Figure 11 plots the a_{wn}^{max} values obtained with the KIS tracer method and with XMT experiments
676 using NAPL-water fluid system from (Culligan et al. 2006; Porter et al. 2010), and air-water fluid
677 system from (Brusseau et al. 2006; Araujo and Brusseau 2020). Likos and Jaafar (2013)
678 developed a pore-geometry model that calculates the specific IFA based on the measured grain-
679 size distributions. They apply their model to four porous media (small glass beads, F75 Ottawa
680 sand, large glass beads, river sand) and plot the capillary-associated IFA, a_{nw} . Note that the
681 capillary-associated IFA determined by Culligan et al. (2006) for air-water and oil-water fluid
682 systems in the same porous medium found the that the capillary-associated IFA for oil-water is
683 larger than that of air-water during main drainage. The surface tension of air-water is higher and
684 the XMT revealed that air phase is located in larger continuous fluid configurations while the oil
685 forms smaller, less well-connected configurations at similar saturations, leading to larger
686 interfacial areas. Here, we do not apply any scaling to a_{wn} values.

687 It is observed that the literature values plotted against the IMGD, follow a linear trend which is
688 larger than the prediction line of a_{wn}^{max} - IMGD obtained from the KIS tracer experiments. The
689 theoretically determined a_{wn}^{max} values using the (Grant and Gerhard 2007) model (illustrated in
690 **Figure 9**, dashed black curves) are in good agreement with the regression line applied through
691 the literature values. For the n-octane-water fluid system the capillary-associated IFA, a_{wn}^{max}
692 determined by KIS tracers ranges between 3.00 ($d_{50}=55 \mu\text{m}$) and 4.64 ($d_{50}=250 \mu\text{m}$) times
693 smaller than the capillary associated IFA reported in the literature. The explanation for this
694 behavior is that the KIS tracer method only measures the mobile fraction of the fluid-fluid
695 interface, which correspond to the mobile terminal menisci displacing the water in the
696 system(Figure 1).



697
 698 **Figure 11:** Mobile a_{wn}^{max} determined by KIS tracer experiment in an n-octane-water fluid system
 699 and comparison with literature data for capillary associated interfacial area.

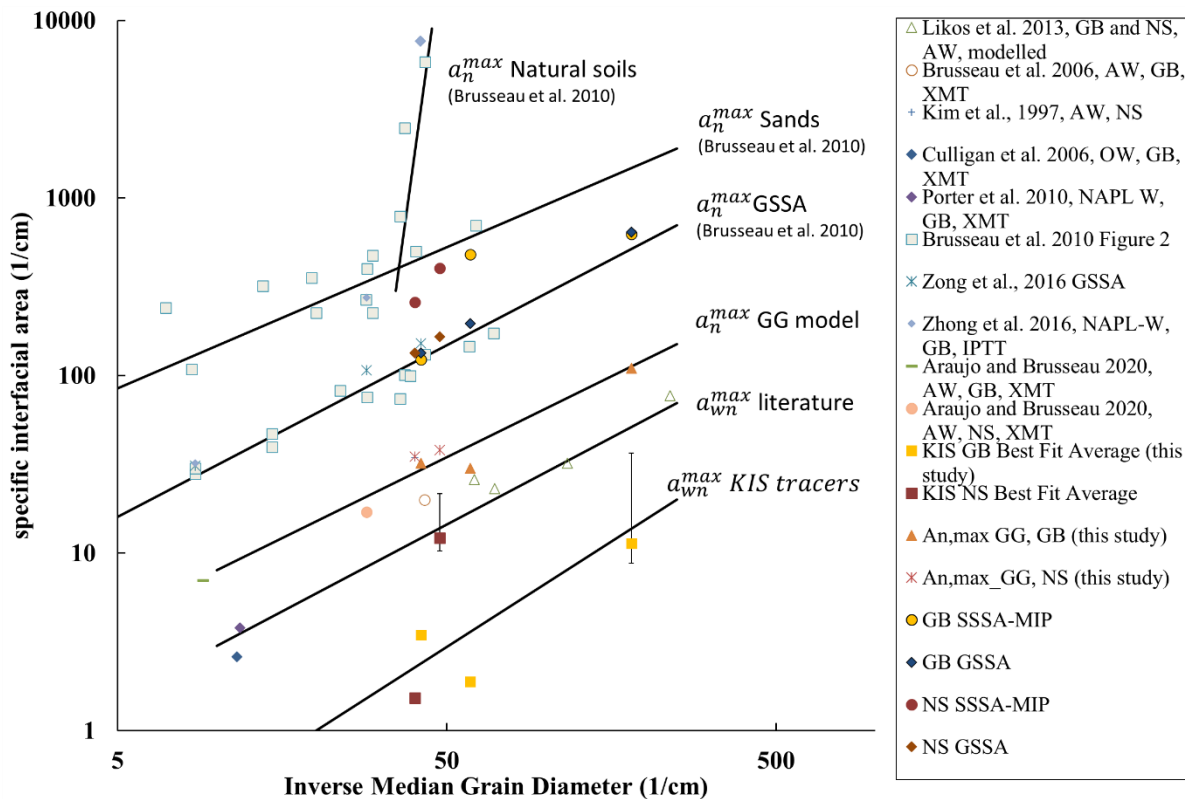
700 **4.3.3 Comparison of total specific interfacial area with literature data**

701 Direct evaluation of the influence of grain diameters, their surface area and their fluid-fluid
 702 interfaces is difficult to perform for the entire set of published data because of the different types
 703 of surface area information reported, and because reported experiments are conducted with
 704 different types of fluid-porous media systems, e.g. air-water, NAPL-water, organic-liquid -water,
 705 etc. With very few exceptions, the literature compiled data contain IFA measured under residual-
 706 saturation conditions, i.e. imbibition conditions. Note, the interfacial area obtained for imbibition
 707 conditions is smaller.

708 Specific fluid-fluid interfaces reported in Brusseau et al. (2009; 2010) for organic-liquid-water
 709 fluid systems and at further data from (Kim et al. 1997; Zhong et al. 2016; Araujo and Brusseau
 710 2020) are plotted against the inverse mean grain diameter on a log-log scale (Figure 12). It is

711 apparent that the general trend for all interfacial areas, a_{wn}^{max} , the a_{wn}^{max} measured by the KIS
 712 tracers, a_n^{max} , and a_n^{max} calculated with the geometric-based smooth sphere approach (GSSA)
 713 can be expressed as linear functions increasing with IMGD. The calculated total specific solid
 714 surface areas with the (Rootare and Prenzlou 1967) model applied to the MIP data match closely
 715 the linear trend reported values from the literature. For the two natural sands the a_n^{max} values (NS
 716 SSSA-MIP) are higher than the corresponding GSSA.

717 It can be observed that the total maximum IFA, a_n^{max} predicted by the (Grant and Gerhard 2007)
 718 model corresponding to the best fitted $a_{wn} - S_w$ curves for the five porous media are smaller
 719 than the linear trend of a_n^{max} of porous media with surface roughness from literature (Brusseau et
 720 al. 2010), and also smaller than the porous media with no surface roughness, or calculated with
 721 the GSSA (Brusseau et al. 2010). On the log-log scale, the linear functions are approximately
 722 parallel to each other. A much steeper increase of the a_n^{max} with IMGD is observed for the
 723 category of natural soils.



724
 725 **Figure 12:** Compiled total specific IFA, a_n , and capillary-associated IFA, a_{wn}^{max} from the
 726 literature and this study. The total IFA for the five materials calculated as SSSA-MIP and GSSA,
 727 and the mobile capillary-associated IFAs determined with KIS tracer method

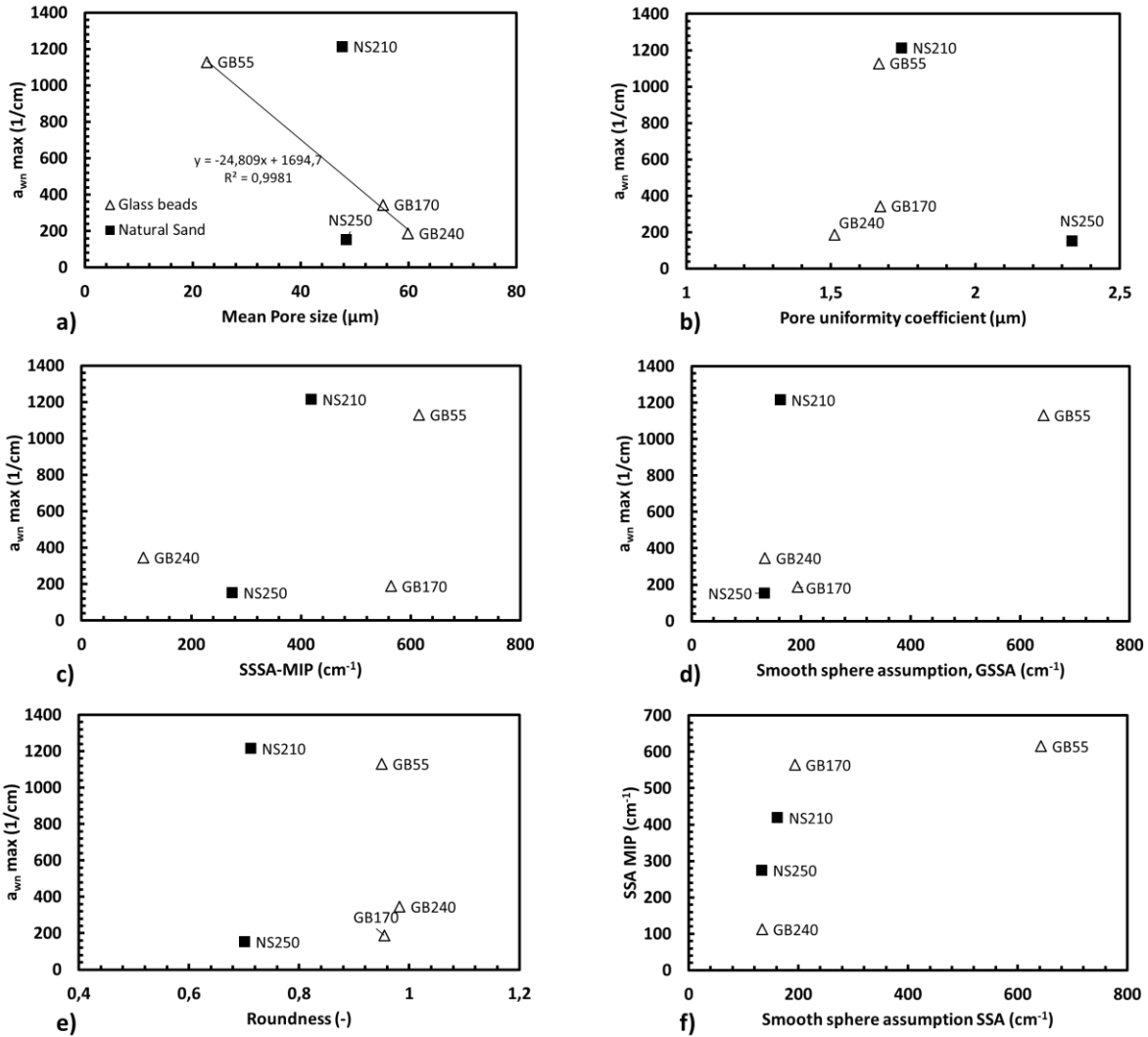
728 4.4 Texture influence on IFA

729 Here, we investigate the influence on a_{wn}^{max} of texture parameters: mean pore size, pore-
 730 uniformity coefficient, specific solid surface area, SSA geometrically calculated (GSSA), and
 731 grain roundness (Figure 13). A higher solid surface area, which incorporates a higher solid
 732 surface roughness, is correlated to a higher specific IFA. For the five porous media, mean pore-
 733 sizes (measured with MIP) correlate well with the mean grain size (measured with DIA) (Figure

734 4). Therefore, when plotting a_{wn}^{max} with the mean pore size (Figure 13a) we see that the larger the
735 mean pore-size the smaller the capillary-associated IFA.

736 The pore-size distribution is reflected in the pore-uniformity coefficient. Figure 13b) shows the
737 influence on C_{pu} on a_{wn}^{max} . The specific solid-grain surface areas of the five materials were
738 derived from the MIP measurements by applying the (Rootare and Prenzlów 1967) model, i.e.,
739 SSSA-MIP, and were also calculated geometrically using the smooth sphere assumption, i.e.
740 GSSA. Their influence on the a_{wn}^{max} is plotted in Figure 13c) and d). In most literature studies the
741 specific solid surface is measured with N₂/BET technique which commonly measures larger
742 values than the SSSA-MIP and GSSA, e.g.(Narter and Brusseau 2010).

743 Generally, it can be concluded that the larger the SSSA the larger the a_{wn}^{max} . The very fine glass
744 beads medium GB55 and the NS210 have the highest SSSA and the highest a_{wn}^{max} (**Table 1**).
745 GB55 has the highest SSSA close to the GSSA value, 643 μm . GB55 resulting a_{wn}^{max} , is slightly
746 smaller than the NS210 which has a large SSSA, measured by MIP. This is a further
747 demonstration that the KIS tracer method can provide a robust characterization technique of
748 fluid-fluid IFA, determine correctly the mobile capillary-associated IFA, since the same trend as
749 in the literature is found. Similar to the findings of (Brusseau et al. 2009) for total FFA, other
750 texture parameters such as the grain- and pore-size distributions, roundness, Feret diameter, have
751 minimal impact on the mobile capillary-associated IFA.



752
 753 **Figure 13:** Specific capillary-associated IFA variation depending on the texture related
 754 parameters.

755 5 Conclusions

756 • We demonstrated that the KIS tracers allow studying the moving fluid-fluid interfaces in
 757 complex three-dimensional systems. On the basis of 15 sets of measurements performed on five
 758 different porous media, we were able to test and successfully extend the range of applicability of
 759 the KIS tracers, previously applied only to one type of glass-beads material. We were able to
 760 determine the specific capillary associated IFA and its linear relationship with the IMGD. We
 761 also observed new phenomena in the tracer BTC, not predicted by Darcy-scale coupled
 762 multiphase flow and reactive-transport models.

763 • The KIS tracer method can serve as a technique to improve our predictive capability of
 764 existing numerical schemes in constraining inverse models. The experimental results constitute
 765 an important data-set regarding the fate of an interface-depending reactive contaminant. The
 766 discrepancy between the experimental results and the numerical approaches underlines the
 767 limitation of existing approaches to fully resolve the processes taking place in the pore space. By

768 using the quantitative results obtained by the experiments, a future perspective is to attempt to
769 match those by means of tuning average properties, like tortuosity, coordination number, while
770 keeping in mind the processes affected by the pore geometry itself, e.g., non-Fickian transport.

771 • KIS tracer measured maximum specific FIFA magnitude increases linearly with inverse
772 mean grain diameter, following a similar trend like the one reported in the literature (Costanza-
773 Robinson and Brusseau 2002; Brusseau et al. 2009; Brusseau et al. 2010) obtained with other
774 methods, e.g., IPTT and XMT. However, the values measured with the KIS tracer method range
775 between 3.00 and 4.64 times smaller than the maximum capillary-associated IFA including both
776 mobile and immobile parts, and, as expected, smaller than the total FIFA, a_n^{max} . The explanation
777 for this observation is that the concentration of the reacted KIS tracer at the outflow is composed
778 only of the solute transported with the mobile part of the water. Some fraction of the reacted
779 solute becomes trapped in stagnant flow regions and it is never measured (to these add up the
780 terminal menisci, pendular ring/ wedge menisci).

781 • We provide a compilation of the literature reported data for the specific fluid-fluid
782 interfaces. Comparison of the measured and interpreted data herein with literature data provides
783 further insights into the characterization of the fluid-fluid /NAPL-water interfaces. Similar to the
784 observations made for the total specific interfacial area, natural sands, with higher roughness lead
785 to larger capillary-associated IFA than the smooth glass beads. Other than the solid surface area
786 we cannot make any conclusive statement about the influence on capillary-associated IFA of the
787 other texture related parameters, e.g. grain- and pore-size distribution, uniformity coefficients,
788 roundness, etc.

789 • The current continuum-scale (Darcy-scale) numerical models for reactive transport in
790 two-phase flow in porous media need to be reconsidered. Many of the experimental breakthrough
791 curves exhibit an early concentration peak and are flattening or decreasing towards the end of the
792 drainage process. Current multiphase-flow models with reactive transport are unable to reproduce
793 these effects. Therefore, to improve the predictive modelling capacities a new theoretical
794 modeling framework is required.

795 • The micro-scale mechanisms need to be investigated separately with pore-scale and pore-
796 network modelling of the reactive-transport and multiphase-flow-coupled processes. A promising
797 approach to interpret the KIS tracer BTCs uses a pore-scale reactive transport model developed
798 by Gao et al. (2020).

799 • For the future, the measurement accuracy of the KIS tracer method should be improved
800 by adding pressure sensors to acquire information regarding the pressure change during the
801 experiment, precise control of the flow rates attainable with high-precision pumps, development
802 of a continuous sampling method to remove the errors during sampling.

803 • In addition, further research is needed to extend the applicability of the method to a wider
804 range of flow conditions and fluid-fluid-porous media systems, e.g., natural soils, soils with
805 wider variety of diameters and textures.

806 Until now the KIS tracer method has not been compared against another measurement technique.
807 KIS tracers have the potential to be applied as a complementary technique for measuring FIFA.
808 In this way, the mobile and the immobile parts of the capillary-associated IFA can be identified,
809 or one can differentiate between mobile and immobile flow regions. This study represents an
810 important step towards establishing KIS tracers as a robust characterization technique capable of
811 measuring fluid-fluid interfacial area in multiphase flow in porous media systems.

812 **Acknowledgments**

813 This project was funded by the German Research Foundation, DFG, under project number 428614366, the
814 European Community's 7th Framework Programme FP7 under grant number 309067 (trust-co2.org), and
815 Horizon 2020 Research and Innovation Programme, FracRisk project
816 (<https://ec.europa.eu/inea/en/horizon-2020/projects/H2020-Energy/Shale-gas/FracRisk>) under grant
817 number 636811. We are grateful for the support of SFB1313 Collaborative Research Center (Project
818 Number 327154368). We are also grateful to Florian Duschl and Dejian Zhou for the support with the
819 laboratory work.

820

821

822 **6 References**

823

824 Annable MD, Rao PSC, Hatfield K, Graham WD, Wood AL, Enfield CG (1998) Partitioning Tracers for
825 Measuring Residual NAPL: Field-Scale Test Results. *J Environ Eng* 124:498–503 .
826 [https://doi.org/10.1061/\(ASCE\)0733-9372\(1998\)124:6\(498\)](https://doi.org/10.1061/(ASCE)0733-9372(1998)124:6(498))

827 Anwar AHMF, Bettahar M, Matsubayashi U (2000) A method for determining air–water interfacial area in
828 variably saturated porous media. *J Contam Hydrol* 43:129–146 . [https://doi.org/10.1016/S0169-7722\(99\)00103-5](https://doi.org/10.1016/S0169-7722(99)00103-5)
829

830 Araujo JB, Brusseau ML (2020) Assessing XMT-Measurement Variability of Air-Water Interfacial Areas in
831 Natural Porous Media. *Water Resour Res* 56:e2019WR025470 .
832 <https://doi.org/10.1029/2019WR025470>

833 Bradford SA, Leij FJ (1997) Estimating interfacial areas for multi-fluid soil systems. *J Contam Hydrol*
834 27:83–105 . [https://doi.org/10.1016/S0169-7722\(96\)00048-4](https://doi.org/10.1016/S0169-7722(96)00048-4)

835 Brooks RH, Corey AT (1964) Hydraulic properties of porous media. *Hydrol Pap No 3 3*:

836 Brusseau ML (2018) Assessing the potential contributions of additional retention processes to PFAS
837 retardation in the subsurface. *Sci Total Environ* 613–614:176–185 .
838 <https://doi.org/10.1016/j.scitotenv.2017.09.065>

839 Brusseau ML (2019) The influence of molecular structure on the adsorption of PFAS to fluid-fluid
840 interfaces: Using QSPR to predict interfacial adsorption coefficients. *Water Res* 152:148–158 .
841 <https://doi.org/10.1016/j.watres.2018.12.057>

842 Brusseau ML, Janousek H, Murao A, Schnaar G (2008) Synchrotron X-ray microtomography and
843 interfacial partitioning tracer test measurements of NAPL-water interfacial areas. *Water Resour*
844 *Res* 44:W01411 . <https://doi.org/10.1029/2006WR005517>

845 Brusseau ML, Narter M, Janousek H (2010) Interfacial partitioning tracer test measurements of organic-
846 liquid/water interfacial areas: application to soils and the influence of surface roughness. *Environ*
847 *Sci Technol* 44:7596–7600 . <https://doi.org/10.1021/es101312n>

848 Brusseau ML, Narter M, Schnaar G, Marble J (2009) Measurement and Estimation of Organic-
849 Liquid/Water Interfacial Areas for Several Natural Porous Media. *Environ Sci Technol* 43:3619–
850 3625 . <https://doi.org/10.1021/es8020827>

851 Brusseau ML, Ouni AE, Araujo JB, Zhong H (2015) Novel methods for measuring air–water interfacial area
852 in unsaturated porous media. *Chemosphere* 127:208–213 .
853 <https://doi.org/10.1016/j.chemosphere.2015.01.029>

854 Brusseau ML, Peng S, Schnaar G, Costanza-Robinson MS (2006) Relationships among air-water interfacial
855 area, capillary pressure, and water saturation for a sandy porous medium. *Water Resour Res*
856 42:W03501 . <https://doi.org/10.1029/2005WR004058>

- 857 Brusseau ML, Peng S, Schnaar G, Murao A (2007) Measuring Air–Water Interfacial Areas with X-ray
858 Microtomography and Interfacial Partitioning Tracer Tests. *Environ Sci Technol* 41:1956–1961 .
859 <https://doi.org/10.1021/es061474m>
- 860 Cary JW (1994) Estimating the surface area of fluid phase interfaces in porous media. *J Contam Hydrol*
861 15:243–248 . [https://doi.org/10.1016/0169-7722\(94\)90029-9](https://doi.org/10.1016/0169-7722(94)90029-9)
- 862 Cho J, Annable MD (2005) Characterization of pore scale NAPL morphology in homogeneous sands as a
863 function of grain size and NAPL dissolution. *Chemosphere* 61:899–908 .
864 <https://doi.org/10.1016/j.chemosphere.2005.04.042>
- 865 Costanza MS, Brusseau ML (2000) Contaminant Vapor Adsorption at the Gas–Water Interface in Soils.
866 *Environ Sci Technol* 34:1–11 . <https://doi.org/10.1021/es9904585>
- 867 Costanza-Robinson MS, Brusseau ML (2002) Air-water interfacial areas in unsaturated soils: Evaluation of
868 interfacial domains. *Water Resour Res* 38:1195 . <https://doi.org/10.1029/2001WR000738>
- 869 Culligan KA, Wildenschild D, Christensen BSB, Gray WG, Rivers ML (2006) Pore-scale characteristics of
870 multiphase flow in porous media: A comparison of air–water and oil–water experiments. *Adv*
871 *Water Resour* 29:227–238 . <https://doi.org/10.1016/j.advwatres.2005.03.021>
- 872 Dalla E, Hilpert M, Miller CT (2002) Computation of the interfacial area for two-fluid porous medium
873 systems. *J Contam Hydrol* 56:25–48
- 874 Dobson R, Schroth MH, Oostrom M, Zeyer J (2006) Determination of NAPL–Water Interfacial Areas in
875 Well-Characterized Porous Media. *Environ Sci Technol* 40:815–822 .
876 <https://doi.org/10.1021/es050037p>
- 877 Flemisch B, Darcis M, Erbertseder K, Faigle B, Lauser A, Mosthaf K, Müthing S, Nuske P, Tatomir A, Wolff
878 M, Helmig R (2011) DuMux: DUNE for multi-{phase, component, scale, physics, ...} flow and
879 transport in porous media. *Adv Water Resour* 34:1102–1112 .
880 <https://doi.org/10.1016/j.advwatres.2011.03.007>
- 881 Fukunishi Y, Tateishi T, Suzuki M (1996) Octane/Water Interfacial Tension Calculation by Molecular
882 Dynamics Simulation. *J Colloid Interface Sci* 180:188–192 .
883 <https://doi.org/10.1006/jcis.1996.0288>
- 884 Gao H, Tatomir AB, Karadimitriou NK, Steeb H, Sauter M (2020) A two-phase, pore-scale reactive
885 transport model for the kinetic interface- sensitive tracer (to be submitted). *Water Resour Res*
- 886 Grant GP, Gerhard JI (2007) Simulating the dissolution of a complex dense nonaqueous phase liquid
887 source zone: 1. Model to predict interfacial area. *Water Resour Res* 43:W12410 .
888 <https://doi.org/10.1029/2007WR006038>
- 889 Gvirtzman H, Roberts PV (1991) Pore scale spatial analysis of two immiscible fluids in porous media.
890 *Water Resour Res* 27:1165–1176 . <https://doi.org/10.1029/91WR00303>
- 891 Hassanizadeh SM, Gray WG (1993) Thermodynamic basis of capillary pressure in porous media. *Water*
892 *Resour Res* 29:3389–3405 . <https://doi.org/10.1029/93WR01495>

- 893 Hassanizadeh SM, Gray WG (1990) Mechanics and thermodynamics of multiphase flow in porous media
894 including interphase boundaries. *Adv Water Resour* 13:169–186 . [https://doi.org/10.1016/0309-1708\(90\)90040-B](https://doi.org/10.1016/0309-1708(90)90040-B)
895
- 896 Heiß VI, Neuweiler I, Ochs S, Färber A (2011) Experimental investigation on front morphology for two-
897 phase flow in heterogeneous porous media. *Water Resour Res* 47:W10528 .
898 <https://doi.org/10.1029/2011WR010612>
- 899 Held RJ, Celia MA (2001) Pore-scale modeling extension of constitutive relationships in the range of
900 residual saturations. *Water Resour Res* 37:165–170 . <https://doi.org/10.1029/2000WR900234>
- 901 Hilfer R, Øren PE (1996) Dimensional analysis of pore scale and field scale immiscible displacement.
902 *Transp Porous Media* 22:53–72 . <https://doi.org/10.1007/BF00974311>
- 903 Jiang H, Guo B, Brusseau ML (2020) Pore-Scale Modeling of Fluid-Fluid Interfacial Area in Variably
904 Saturated Porous Media Containing Microscale Surface Roughness. *Water Resour Res*
905 56:e2019WR025876 . <https://doi.org/10.1029/2019WR025876>
- 906 Joekar-Niasar V, Hassanizadeh SM (2012a) Analysis of Fundamentals of Two-Phase Flow in Porous Media
907 Using Dynamic Pore-Network Models: A Review. *Crit Rev Environ Sci Technol* 42:1895–1976 .
908 <https://doi.org/10.1080/10643389.2011.574101>
- 909 Joekar-Niasar V, Hassanizadeh SM (2012b) Uniqueness of Specific Interfacial Area–Capillary Pressure–
910 Saturation Relationship Under Non-Equilibrium Conditions in Two-Phase Porous Media Flow.
911 *Transp Porous Media* 94:465–486 . <https://doi.org/10.1007/s11242-012-9958-3>
- 912 Karadimitriou NK, Joekar-Niasar V, Babaei M, Shore CA (2016) Critical Role of the Immobile Zone in Non-
913 Fickian Two-Phase Transport: A New Paradigm. *Environ Sci Technol* 50:4384–4392 .
914 <https://doi.org/10.1021/acs.est.5b05947>
- 915 Kim H, Rao PSC, Annable MD (1997) Determination of effective air-water interfacial area in partially
916 saturated porous media using surfactant adsorption. *Water Resour Res* 33:2705 .
917 <https://doi.org/10.1029/97WR02227>
- 918 Kim H, Rao PSC, Annable MD (1999) Gaseous Tracer Technique for Estimating Air–Water Interfacial Areas
919 and Interface Mobility. *Soil Sci Soc Am J* 63:1554–1560 .
920 <https://doi.org/10.2136/sssaj1999.6361554x>
- 921 Lenormand R, Touboul E, Zarcone C (1988) Numerical models and experiments on immiscible
922 displacements in porous media. *J Fluid Mech* 189:165–187 .
923 <https://doi.org/10.1017/S0022112088000953>
- 924 Leverett MC (1941) Capillary Behavior in Porous Solids. *Trans AIME* 142:152–169 .
925 <https://doi.org/10.2118/941152-G>
- 926 Likos WJ, Jaafar R (2013) Pore-Scale Model for Water Retention and Fluid Partitioning of Partially
927 Saturated Granular Soil. *J Geotech Geoenvironmental Eng* 139:724–737 .
928 [https://doi.org/10.1061/\(ASCE\)GT.1943-5606.0000811](https://doi.org/10.1061/(ASCE)GT.1943-5606.0000811)

- 929 Lyu Ying, Brusseau Mark L., El Ouni Asma, Araujo Juliana B., Su Xiaosi (2017) The Gas-
930 Absorption/Chemical-Reaction Method for Measuring Air-Water Interfacial Area in Natural
931 Porous Media. *Water Resour Res* 53:9519–9527 . <https://doi.org/10.1002/2017WR021717>
- 932 McDonald K, Carroll KC, Brusseau ML (2016) Comparison of fluid-fluid interfacial areas measured with X-
933 ray microtomography and interfacial partitioning tracer tests for the same samples. *Water*
934 *Resour Res* 52:5393–5399 . <https://doi.org/10.1002/2016WR018775>
- 935 Miller CT, Poirier-McNeil MM, Mayer AS (1990) Dissolution of Trapped Nonaqueous Phase Liquids: Mass
936 Transfer Characteristics. *Water Resour Res* 26:2783–2796 .
937 <https://doi.org/10.1029/WR026i011p02783>
- 938 Narter M, Brusseau ML (2010) Comparison of Interfacial partitioning tracer test and high-resolution
939 microtomography measurements of fluid-fluid interfacial areas for an ideal porous medium.
940 *Water Resour Res* 46: . <https://doi.org/10.1029/2009WR008375>
- 941 Nelson NT, Brusseau ML (1996) Field Study of the Partitioning Tracer Method for Detection of Dense
942 Nonaqueous Phase Liquid in a Trichloroethene- Contaminated Aquifer. *Environ Sci Technol*
943 30:2859–2863 . <https://doi.org/10.1021/es960148b>
- 944 Niemi A, Bensabat J, Shtivelman V, Edlman K, Gouze P, Luguot L, Hingl F, Benson SM, Pezard P,
945 Rasmusson K, Tian L, Fagerlund F, Tatomir AB, Lange, Torsten, Sauter M, Freifeld B (2016)
946 Overview of the Heletz site, its characterization and data analysis for CO₂ injection and
947 geological storage (submitted). *Int J Greenh Gas Control* xx:
- 948 Oostrom M, White MD, Brusseau ML (2001) Theoretical estimation of free and entrapped nonwetting–
949 wetting fluid interfacial areas in porous media. *Adv Water Resour* 24:887–898 .
950 [https://doi.org/10.1016/S0309-1708\(01\)00017-3](https://doi.org/10.1016/S0309-1708(01)00017-3)
- 951 Patmonoaji A, Tsuji K, Muharrik M, Suekane T (2018) Micro-tomographic analyses of specific interfacial
952 area inside unconsolidated porous media with differing particle characteristics from microscopic
953 to macroscopic scale. *J Colloid Interface Sci* 532:614–621 .
954 <https://doi.org/10.1016/j.jcis.2018.08.023>
- 955 Peche A, Halisch M, Bogdan Tatomir A, Sauter M (2016) Development of a numerical workflow based on
956 μ -CT imaging for the determination of capillary pressure–saturation-specific interfacial area
957 relationship in 2-phase flow pore-scale porous-media systems: a case study on Heletz sandstone.
958 *Solid Earth* 7:727–739 . <https://doi.org/10.5194/se-7-727-2016>
- 959 Peng S, Brusseau ML (2005) Impact of soil texture on air-water interfacial areas in unsaturated sandy
960 porous media. *Water Resour Res* 41: . <https://doi.org/10.1029/2004WR003233>
- 961 Porter ML, Wildenschild D, Grant G, Gerhard JI (2010) Measurement and prediction of the relationship
962 between capillary pressure, saturation, and interfacial area in a NAPL-water-glass bead system.
963 *Water Resour Res* 46:W08512 . <https://doi.org/10.1029/2009WR007786>
- 964 Reeves PC, Celia MA (1996) A Functional Relationship Between Capillary Pressure, Saturation, and
965 Interfacial Area as Revealed by a Pore-Scale Network Model. *Water Resour Res* 32:2345 .
966 <https://doi.org/10.1029/96WR01105>

- 967 Rootare HM, Prenzlou CF (1967) Surface areas from mercury porosimeter measurements. *J Phys Chem*
968 71:2733–2736 . <https://doi.org/10.1021/j100867a057>
- 969 Saripalli KP, Kim H, Rao PSC, Annable MD (1997) Measurement of Specific Fluid–Fluid Interfacial Areas of
970 Immiscible Fluids in Porous Media. *Environ Sci Technol* 31:932–936 .
971 <https://doi.org/10.1021/es960652g>
- 972 Schaefer CE, DiCarlo DA, Blunt MJ (2000) Determination of Water-Oil Interfacial Area during 3-Phase
973 Gravity Drainage in Porous Media. *J Colloid Interface Sci* 221:308–312 .
974 <https://doi.org/10.1006/jcis.1999.6604>
- 975 Schaffer M, Maier F, Licha T, Sauter M (2013) A new generation of tracers for the characterization of
976 interfacial areas during supercritical carbon dioxide injections into deep saline aquifers: Kinetic
977 interface-sensitive tracers (KIS tracer). *Int J Greenh Gas Control* 14:200–208 .
978 <https://doi.org/10.1016/j.ijggc.2013.01.020>
- 979 Schnaar G, Brusseau ML (2006) Characterizing Pore-Scale Configuration of Organic Immiscible Liquid in
980 Multiphase Systems With Synchrotron X-Ray Microtomography. *Vadose Zone J* 5:641–648 .
981 <https://doi.org/10.2136/vzj2005.0063>
- 982 Simon MA, Brusseau ML (2007) Analysis of a gas-phase partitioning tracer test conducted in an
983 unsaturated fractured-clay formation. *J Contam Hydrol* 90:146–158 .
984 <https://doi.org/10.1016/j.jconhyd.2006.09.010>
- 985 Tatomir A, Maier F, Schaffer M, Licha T, Sauter M (2013) Modelling of Kinetic Interface Sensitive Tracers
986 for Two-Phase Systems. In: Hou MZ, Xie H, Were P (eds) *Clean Energy Systems in the Subsurface: Production, Storage and Conversion*. Springer Berlin Heidelberg, pp 65–74
- 988 Tatomir A, Vriendt KD, Zhou D, Gao H, Duschl F, Sun F, Licha T, Sauter M (2018) Kinetic Interface
989 Sensitive Tracers: Experimental Validation in a Two-Phase Flow Column Experiment. A Proof of
990 Concept. *Water Resour Res* 54:10,223–10,241 . <https://doi.org/10.1029/2018WR022621>
- 991 Tatomir AB, Halisch M, Duschl F, Peche A, Wiegand B, Schaffer M, Licha T, Niemi A, Bensabat J, Sauter M
992 (2016a) An integrated core-based analysis for the characterization of flow, transport and
993 mineralogical parameters of the Heletz pilot CO₂ storage site reservoir. *Int J Greenh Gas Control*
994 48, Part 1:24–43 . <https://doi.org/10.1016/j.ijggc.2016.01.030>
- 995 Tatomir AB, Jyoti A, Sauter M (2016b) The Monitoring of CO₂ plume migration in deep saline formations
996 with kinetic interface sensitive tracers. In: Singh TN, Vikram V (eds) *Geologic Carbon Sequestration: Understanding Reservoir Concepts*. Springer, p 336
- 998 Tatomir AB, Schaffer M, Kissinger A, Hommel J, Nuske P, Licha T, Helmig R, Sauter M (2015) Novel
999 approach for modeling kinetic interface-sensitive (KIS) tracers with respect to time-dependent
1000 interfacial area change for the optimization of supercritical carbon dioxide injection into deep
1001 saline aquifers. *Int J Greenh Gas Control* 33:145–153 .
1002 <https://doi.org/10.1016/j.ijggc.2014.11.020>
- 1003 Washburn EW (1921) Note on a Method of Determining the Distribution of Pore Sizes in a Porous
1004 Material. *Proc Natl Acad Sci U S A* 7:115–116

1005 Zhong H, El Ouni A, Lin D, Wang B, Brusseau ML (2016) The two-phase flow IPTT method for
1006 measurement of nonwetting-wetting liquid interfacial areas at higher nonwetting saturations in
1007 natural porous media. *Water Resour Res* 52:5506–5515 .
1008 <https://doi.org/10.1002/2016WR018783>

1009

1010

1011 **7 Appendix**

1012

1013

1014

1015
1016

Table SI 1. Best fitting parameters for the modelling of the KIS tracer experiments: 1) calibration of the volume ratio of the n-octane and water; 2) calibration of the 2-NSA concentration BTC.

Experiment index	Volume ratio V_n/V_T BTC							2-NSA Concentration BTC			S_w at end of experiment	
	Q_{\min} (ml/min)	Q_{\max} (ml/min)	Q_{BF} (ml/min)	K_{\min} (m ²)	K_{\max} (m ²)	K_{BF} (m ²)	RMSE	a_0	a_{wn}^{max} (m ⁻¹)	RMSE	Experiment	Model
GB55_1	0.6	0.64	0.61	2×10^{-13}	6×10^{-13}	6×10^{-13}	0.045241	1×10^{-5}	848	0.3162	0.18	0.36
GB55_3	0.54	0.58	0.55	1×10^{-13}	5×10^{-13}	5×10^{-13}	0.009795	1.5×10^{-5}	1270	1.2831	0.16	0.37
GB55_4	0.56	0.60	0.57	4×10^{-13}	8×10^{-13}	8×10^{-13}	0.026996	1.5×10^{-5}	1270	0.8899	0.2	0.37
GB170_2	0.53	0.57	0.55	8×10^{-13}	12×10^{-13}	1.1×10^{-12}	0.05649	5×10^{-6}	141	0.5561	0.26	0.35
GB170_3	0.67	0.71	0.68	5.8×10^{-12}	6.2×10^{-12}	6×10^{-12}	0.052176	5×10^{-6}	141	0.5145	0.27	0.36
GB170_6	0.62	0.66	0.62	3.0×10^{-12}	7.0×10^{-12}	5×10^{-12}	0.0129	1×10^{-5}	282	1.5397	0.28	0.35
GB240_1	0.42	0.46	0.44	1.0×10^{-12}	5.0×10^{-12}	2×10^{-12}	0.018418	2×10^{-5}	519	2.3039	0.27	0.36
GB240_2	0.65	0.68	0.65	4.0×10^{-12}	6.0×10^{-12}	4×10^{-12}	0.018708	1×10^{-5}	260	1.839	0.35	0.35
GB240_3	0.66	0.70	0.66	1.0×10^{-12}	5.0×10^{-12}	4×10^{-12}	0.023005	1×10^{-5}	260	1.5397	0.31	0.36
NS210_3	0.60	0.64	0.62	5.0×10^{-13}	9.0×10^{-13}	8×10^{-13}	0.0289	4×10^{-5}	1120	1.0787	0.35	0.38
NS210_4	0.62	0.66	0.65	7.0×10^{-13}	11×10^{-13}	8×10^{-13}	0.01687	3×10^{-5}	841	0.8517	0.38	0.37
NS210_5	0.61	0.65	0.64	4.0×10^{-13}	8.0×10^{-13}	6×10^{-13}	0.023323	6×10^{-5}	1680	0.5484	0.32	0.37
NS250_1	0.70	0.74	0.73	5.0×10^{-12}	9.0×10^{-12}	5×10^{-12}	0.0133	1×10^{-5}	241	1.3005	0.44	0.39
NS250_2	0.76	0.80	0.76	5.0×10^{-12}	9.0×10^{-12}	9×10^{-12}	0.015451	5×10^{-5}	121	1.6447	0.43	0.43
NS250_3	0.46	0.50	0.46	1.0×10^{-12}	5.0×10^{-12}	3×10^{-12}	0.017759	4×10^{-5}	96.5	0.9524	0.48	0.43

1017

1018 To calculate the capillary number for the Darcy-scale column experiments we apply the following
 1019 transformation (Hilfer and Øren 1996):

$$Ca = \frac{\mu_i v_D L}{p_d K}$$

1020 where μ_i is the dynamic viscosity of the invading fluid, v_D is the mean Darcy velocity of the
 1021 invading fluid, p_d is the entry pressure of the nonwetting fluid into the porous material, and K is
 1022 the intrinsic permeability.

1023 **Table SI 2. Calculated capillary number, Ca**

Experiment	K (m^2)	ϕ (-)	p_d (Pa)	v_D (m/s)	Ca
GB55_1	6E-13	0.411	5937	3.5E-05	1.228
GB55_3	5.00E-13	0.411	5937	3.16E-05	1.329
GB55_4	8.00E-13	0.411	5937	3.27E-05	0.861
GB170_2	1.10E-12	0.455	1819	2.85E-05	1.781
GB170_3	6.00E-12	0.455	1819	3.52E-05	0.404
GB170_6	5.00E-12	0.455	1819	3.21E-05	0.442
GB240_1	2.00E-12	0.464	1606	2.24E-05	0.870
GB240_2	4.00E-12	0.464	1606	3.3E-05	0.643
GB240_3	4.00E-12	0.464	1606	3.35E-05	0.653
NS210_3	8.00E-13	0.432	2050	3.38E-05	2.579
NS210_4	8.00E-13	0.432	2050	3.55E-05	2.704
NS210_5	6.00E-13	0.432	2050	3.49E-05	3.55
NS250_1	5.00E-12	0.445	1642	3.87E-05	0.589
NS250_2	9.00E-12	0.445	1642	4.03E-05	0.341
NS250_3	3.00E-12	0.445	1642	2.44E-05	0.618

1024
 1025 **Table SI 3. Data sets used for the total specific interfacial areas (after Brusseau et al. 2010)**

Porous medium	S_n	No. measurements	Data Source
Vinton Soil	0.15	4	(Brusseau et al. 2010)
Eustis soil	0.17	4	(Brusseau et al. 2010)
Mixed sand	0.26	2	(Brusseau et al. 2008)
45-50 mesh sand	0.17	8	(Brusseau et al. 2008)
12-20 mesh sand	0.29	6	(Dobson et al. 2006)
20-30 mesh sand	0.28	5	(Dobson et al. 2006)
30-40 mesh sand	0.27	6	(Dobson et al. 2006)
40-50 mesh sand	0.28	5	(Dobson et al. 2006)
10-12 mesh sand	0.12	1	(Cho and Annable 2005)
20-30 mesh sand	0.14	1	(Cho and Annable 2005)
30-40 mesh sand	0.12	1	(Cho and Annable 2005)
40-60 mesh sand	0.15	1	(Cho and Annable 2005)
80-100 mesh sand	0.16	1	(Cho and Annable 2005)
40-100 mesh sand	0.19	3	(Saripalli et al. 1997)
40-50 mesh sand	Variable	5	(Schaefer et al. 2000)

1026 S_n - saturation of organic liquid

